Monthly Notices
of the
ROYAL ASTRONOMICAL SOCIETY

MNRAS **486,** 743–767 (2019)
Advance Access publication 2019 March 19

doi:10.1093/mnras/stz805

Revealing the dust attenuation properties on resolved scales in NGC 628 with *SWIFT* UVOT data

Marjorie Decleir [1]★ Ilse De Looze,[1,2]★ Médéric Boquien,[3]★ Maarten Baes [1] Sam Verstocken,[1] Daniela Calzetti,[4] Laure Ciesla,[5] Jacopo Fritz [6] Rob Kennicutt,[7] Angelos Nersesian[1,8,9] and Mathew Page[10]

[1]*Sterrenkundig Observatorium, Universiteit Gent, Krijgslaan 281 S9, B-9000 Gent, Belgium*
[2]*Department of Physics and Astronomy, University College London, Gower Street, London WC1E 6BT, UK*
[3]*Centro de Astronomía (CITEVA), Universidad de Antofagasta, Avenida Angamos 601, Antofagasta 1270300, Chile*
[4]*Department of Astronomy, University of Massachusetts – Amherst, Amherst, MA 01003, USA*
[5]*Laboratoire AIM-Paris-Saclay, CEA/DSM/Irfu-CNRS-Université Paris Diderot, CEA-Saclay, F-91191 Gif-sur-Yvette, France*
[6]*Instituto de Radioastronomía y Astrofísica, UNAM, Campus Morelia, AP 3-72, 58089 Michoacán, Mexico*
[7]*Steward Observatory, University of Arizona, 933 N Cherry Avenue, Tucson, AZ 85721-0065, USA*
[8]*Department of Astrophysics, Astronomy and Mechanics, Faculty of Physics, University of Athens, Panepistimiopolis, GR15784 Zografos, Athens, Greece*
[9]*Institute of Astronomy, Astrophysics, Space Applications and Remote Sensing, National Observatory of Athens, GR15236 Penteli, Greece*
[10]*Mullard Space Science Laboratory, University College London, Holmbury St Mary, Dorking, Surrey RH5 6NT, UK*

Accepted 2019 March 13. Received 2019 January 15; in original form 2018 October 4

ABSTRACT

Understanding how dust attenuation laws vary between and within galaxies is a key question if we want to reliably measure the physical properties of galaxies at both global and local scales. To shed new light on this question, we present a detailed study of the slope and bump strength of the attenuation law in the nearby spiral galaxy NGC 628 at the resolved spatial scale of 325 pc. To do so, we have modelled a broad multiwavelength data set from the ultraviolet (UV) to the infrared (IR) with the state-of-the-art SED fitting code CIGALE, including *SWIFT* UVOT data for which we have developed a new optimized reduction pipeline. We find that the median dust attenuation curve of NGC 628 is fairly steep, but not as steep as the SMC curve, and has a sub-MW-type UV bump. We observe intriguing variations within the galaxy, with regions of high A_V exhibiting a shallower attenuation curve. We argue that the flattening of the curve is due to a dominance of absorption over scattering events at higher A_V. No trend between the bump strength and the IRAC 8.0 μm emission was found. However, this does not necessarily rule out polycyclic aromatic hydrocarbons as the main contributors to the UV bump.

Key words: dust, extinction – galaxies: individual: NGC 628 – galaxies: ISM; techniques: image processing; ultraviolet: ISM.

1 INTRODUCTION

Interstellar dust only makes up a very small fraction of the interstellar mass in galaxies (typically about 1 per cent in metal-rich spirals or less in lower metallicity galaxies, e.g. Rémy-Ruyer et al. 2014). Nevertheless, its impact on the other baryonic components in galaxies should not be underestimated, since dust regulates several physical and chemical processes. For example, dust particles act as a catalyst for the formation of molecular hydrogen (Gould & Salpeter 1963), regulate the heating of the neutral gas component through photoelectric heating (Draine 1978) and inelastic interactions, and provide shielding for molecules from the hard ultraviolet (UV) radiation of young stars (Hirashita & Harada 2017). Furthermore, dust is a reservoir of metals, which are the main building blocks for planet formation, and in fact for all organic materials that we know today. Finally, as dust grains absorb and scatter about 30 per cent of the starlight (UV and optical radiation) in the Universe (Lagache, Puget & Dole 2005; Viaene et al. 2016), they heavily influence our view on the other galaxy components. To obtain an undistorted view of galaxies, understanding the interplay between dust and starlight is essential.

It is important at this point to stress the difference between extinction and attenuation. Extinction is caused by dust absorption and scattering out of the line of sight. Extinction curves describe these

★ E-mail: marjorie.decleir@ugent.be (MD); ilse.delooze@ugent.be (IDL); mederic.boquien@uantof.cl (MB)

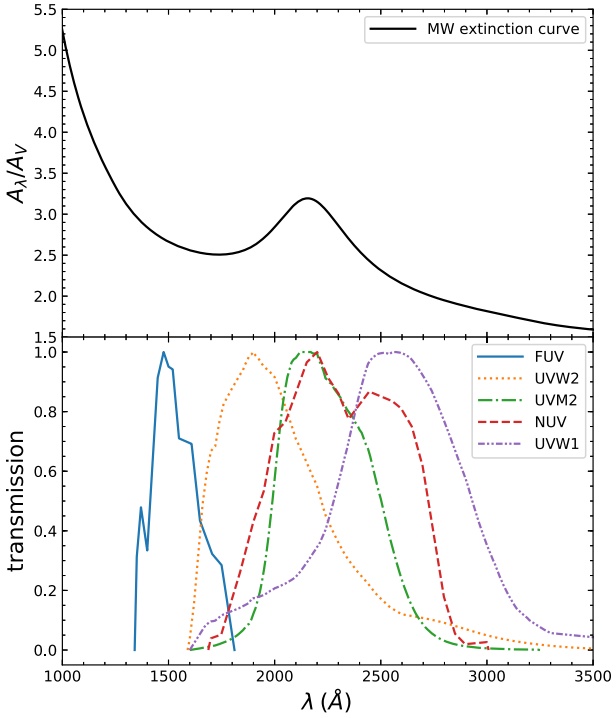

Figure 1. Transmission curves of the *SWIFT* UV filters and the *GALEX* filters, taken from the SVO Filter Profile Service. Rodrigo, C., Solano, E., Bayo, A. http://ivoa.net/documents/Notes/SVOFPS/index.html. The Filter Profile Service Access Protocol. Rodrigo, C., Solano, E. http://ivoa.net/documents/Notes/SVOFPSDAL/index.html. (http://svo2.cab.inta-csic.es/svo/theory/fps/). The MW extinction curve in the top panel is taken from Cardelli et al. (1989).

effects of dust on the galaxy's luminosity at different wavelengths for the specific geometry of a single star behind a screen of dust. For all other geometries, the effect of dust can be described by a dust attenuation curve, which also includes scattering into the line of sight due to the mix of stars and dust.

The specific shape of a dust extinction (or attenuation) law is characterized by the steepness of its slope in UV, optical, and (near-)infrared (NIR) wavebands, and the strength of the 2175 Å bump (i.e. an excess in dust absorption around that wavelength). Often, the slope is parametrized through the total-to-selective extinction ratio, $R_V = A_V/E(B-V)$, with an average value of $R_V = 3.1$ [in the Milky Way (MW); Cardelli, Clayton & Mathis 1989], and with regions dominated by smaller/larger grains characterized by steeper/shallower slopes (or thus smaller/larger R_V). The steepness of the average Small Magellanic Cloud (SMC) dust law ($R_V = 2.7$, Gordon et al. 2003) is therefore thought to result from a grain population with predominantly smaller grains (Clayton et al. 2003; Cartledge et al. 2005). The bump feature is believed to be caused by small grains with a carbonaceous composition [e.g. polycyclic aromatic hydrocarbons (PAHs) or graphite grains], based on laboratory studies, although an observational link between the abundance of possible bump carriers and bump strength remains to be found (e.g. Hagen et al. 2017). Also, the invariable peak wavelength but changing width of the bump feature (e.g. Valencic, Clayton & Gordon 2004) has been proven hard to reconcile with theoretical calculations (Draine & Malhotra 1993). A strong 2175 Å bump is observed in the MW (see Fig. 1), with considerable variations from one sightline to the other, while only a weak bump is present in the Large Magellanic Cloud (LMC) and it is completely absent in the SMC. Interestingly, dust attenuation laws in starburst galaxies also tend to be characterized by a weak bump or no bump at all (Calzetti et al. 2000). However, in addition to varying grain properties, different geometrical distributions are argued to be able to affect the presence of a bump feature (e.g. Panuzzo et al. 2007).

In Local Group galaxies, dust extinction curves can be inferred from a comparison of two stars of the same spectral type but affected by different levels of extinction (this technique is referred to as the 'pair method'). The diversity of dust extinction laws derived through the pair method along different sightlines (e.g. Gordon et al. 2003; Clayton et al. 2015) is consistent with a non-uniform population of interstellar dust grains in a single galaxy. For galaxies beyond the Local Group, on the other hand, (with the exception of pairs of occulting galaxies, e.g. Holwerda et al. 2013; Keel et al. 2014), we resort to deriving dust attenuation curves, which hold information on both the dust absorption and scattering out of the line of sight (characterized by optical grain properties), and the process of scattering into the line of sight (dependent on the relative star–dust geometry). As nicely summarized by Salim, Boquien & Lee (2018), dust attenuation curves are typically inferred using two distinct methods; either through a statistical 'empirical' comparison of large samples of galaxies with different levels of extinction (assuming that the average dust attenuation law does not vary significantly among galaxies), or alternatively through a 'model' comparison of the observed stellar radiation with models of stellar populations attenuated by a range of dust attenuation laws. Due to the computational cost of this last 'model' method, the first dust attenuation curves have been inferred based on the 'empirical' comparison method (e.g. Calzetti, Kinney & Storchi-Bergmann 1994; Calzetti et al. 2000). Similar techniques have also been used in more recent works (e.g. Wild et al. 2011; Battisti, Calzetti & Chary 2016, 2017a). Owing to the introduction of Bayesian inference approaches and other statistical methods, capable of doing a rigorous search of the full parameter space, several authors have published 'model'-inferred dust attenuation curves (e.g. Conroy, Schiminovich & Blanton 2010; Buat et al. 2011, 2012; Leja et al. 2017; Salim et al. 2018) in recent years. Intriguingly, the dust attenuation laws inferred from the 'empirical' and 'model' methods do not always agree, and potentially result in very discrepant dust properties. This apparent dichotomy was attributed to the assumption of a uniform dust attenuation law across entire galaxy samples, and the underestimation of dust attenuation for galaxies considered to be completely transparent, in the case of the 'empirical' comparison method (Salim et al. 2018).

Due to a lack of detailed knowledge about the dust properties outside our own Galaxy and the Magellanic Clouds, in extragalactic studies they are generally assumed to be the same as in the MW. Coupling these dust grain properties to different geometries results in different attenuation laws. For normal galaxies, the MW extinction law is usually adopted, while the Calzetti et al. (2000) relation is used for star-bursting galaxies. However, there is growing evidence for strong deviations from a universal dust attenuation law, based on the different shapes of dust attenuation curves observed in other galaxies (e.g. Reddy et al. 2015; Salmon et al. 2016; Battisti et al. 2017a; Battisti, Calzetti & Chary 2017b; Salim et al. 2018). Imprecise assumptions about the shape of the dust attenuation curve, which is dependent on both the dust properties and the relative star–dust geometry, can result in unattenuated stellar luminosities erroneous by a factor of a few (Driver et al. 2007; Buat et al. 2014). Dust attenuation is still one of the most uncertain parameters to

recover intrinsic star formation rates (SFRs), star formation histories (SFHs), dust masses, and stellar masses at all redshifts (Madau & Dickinson 2014).

Statistical studies of large galaxy samples allow us to infer an average dust attenuation law, to study the spread of galaxies from this mean trend, and to understand how the dust attenuation law varies with galaxy properties. However, to understand what physical processes are driving dust evolution on local scales within galaxies, we require spatially resolved studies of the dust attenuation law in a set of nearby galaxies. To this aim, we launched the DustKING project that will study the attenuation curve in the KINGFISH (Key Insights on Nearby Galaxies: a Far-Infrared Survey with Herschel, Kennicutt et al. 2011) sample of 61 well-resolved nearby galaxies, spanning a wide range of morphologies and star formation activities, and thus probing different stages in dust evolution. The KINGFISH sample largely benefits from an extensive ancillary set of imaging and spectroscopy data. In this work, we study the dust attenuation properties on spatially resolved scales of about 325 pc (or 7 arcsec) in NGC 628 (or M74), a nearby ($D \approx 9.59$ Mpc, Kreckel et al. 2017) grand design spiral galaxy in the constellation Pisces. This galaxy has been classified as an SAc spiral galaxy with a stellar mass of $\log(M_*/\mathrm{M}_\odot) = 9.821$, an SFR $= 1.07\,\mathrm{M}_\odot\,\mathrm{yr}^{-1}$, and a metallicity of $12 + \log(O/H) = 8.80$ (Hunt et al. 2018). The main motivation to start with NGC 628 is that it is a well-studied and well-resolved galaxy, for which a lot of ancillary data (including deep *SWIFT* images, see below) are available. Although we are studying the attenuation properties on resolved scales within the galaxy, it should be noted that there might still be large variations in attenuation within each pixel. Since molecular clouds in nearby galaxies are found to be between 4 and 190 pc in radius (Hughes et al. 2013), one resolved region (of about 325 pc) can contain a mix of clouds with different gas and dust properties. This can affect the observed dust attenuation curve.

In our study, we use a multiwavelength data set, ranging from the far-ultraviolet (FUV) to the far-infrared (FIR), as described in more detail in Section 2. In particular, we make use of UV images taken by the *SWIFT* satellite. The *SWIFT* spacecraft (Gehrels et al. 2004) is designed to detect events such as gamma-ray bursts and is, therefore, equipped with three photon-counting instruments that are sensitive to single-photon events of point sources. The Burst Alert Telescope (BAT, 15–150 keV) and the X-ray Telescope (XRT, 0.3–10 keV) focus on detecting high-energy photons, while the UV/Optical Telescope (UVOT, 1700–6000 Å, Roming et al. 2005) probes the stellar emission in the UV/optical wavelength domain. The set of three UVOT near-ultraviolet (*NUV*) broad-band filters (*UVW2*, *UVM2*, and *UVW1* with effective wavelengths of 1991, 2221, and 2486 Å, respectively) are uniquely suited to constrain the attenuation curve. Fig. 1 shows the transmission curves of these filters and the *GALEX FUV* and *NUV* filters, together with an average MW extinction curve. More specifically, the *UVM2* filter overlaps the 2175 Å dust absorption feature, so when the *UVM2* flux is suppressed relative to that of *UVW2* and *UVW1*, the degree of suppression traces the amplitude of the bump. Likewise, the amount of *UVW2* flux that is extinguished compared to *UVW1* helps to trace the slope of the curve, especially when combined with optical and NIR observations (Hagen et al. 2017). Additionally, the images have a high spatial resolution that is twice as good as the resolution of *GALEX*. Since the *SWIFT* telescope is designed to detect point sources, the standard *SWIFT* data reduction pipeline is not suitable for our purposes (i.e. the study of the dust on resolved scales in extended sources such as nearby galaxies). In order to solve this issue, we developed a new reduction pipeline, which is entirely optimized for extended sources. We present our pipeline in Section 3.

The *SWIFT* data have, so far, only been used to study the interstellar dust properties in a handful of nearby galaxies: M81 and Holmberg IX (Hoversten et al. 2011), both exhibiting grain characteristics that are not very different from the MW; the starburst galaxy M82 (Hutton et al. 2014; Hutton, Ferreras & Yershov 2015) that shows a gradient in the dust attenuation properties with projected galactocentric distance; the SMC (Hagen et al. 2017) that seems to have a large-scale gradient in bump strengths; and the central 200 pc of the M31 bulge (Dong et al. 2014), where the extinction curve is found to be steep ($R_V = 2.4$–2.5). Another work by De Looze et al. (in preparation) will do a study similar to ours for M51.

The remainder of this paper is structured as follows. Section 2 describes the data that were used. Sections 3 and 4 focus on the reduction pipeline of the *SWIFT* UVOT data and the further processing of the images, respectively. In Section 5, we discuss empirical UV colour–colour plots. Section 6 explains the modelling of the galaxy with CIGALE and presents our results, which are further discussed and compared to other studies in Section 7. Finally, Section 8 summarizes our study and main results. The appendix of this paper contains the following sections: Appendix A with the IDs of the *SWIFT* UVOT images used in this work, Appendix B with a detailed description on the calculation of the coincidence loss correction for the *SWIFT* UVOT images, Appendix C lists the parameter values used in the CIGALE fitting, Appendix D shows the observations and models of the CIGALE fitting in each waveband, and Appendix E describes the mock data analysis.

2 DATA

In this work, we employ multiwavelength data ranging from the FUV to the FIR, as listed in Table 1. We are not using images with a longer wavelength (which have a poorer resolution) than the PACS 100 μm image since we want to perform our study on the smallest possible resolved scales (of about 7 arcsec). As discussed in the introduction, we use images from the *SWIFT* UVOT instrument for which we developed a new data reduction pipeline optimized for extended sources. More details about the *SWIFT* data and the reduction pipeline are given in Section 3.

The MIPS 24 μm image was obtained from SINGS (Spitzer Infrared Nearby Galaxies Survey) and the data reduction of this image is described in Kennicutt et al. (2003). All other images were taken from the DustPedia Archive,[1] which provides access to multiwavelength imagery and photometry for 875 nearby galaxies as well as model-derived physical parameters for each galaxy (Davies et al. 2017). The DustPedia images were reduced in a homogeneous way as described in detail in Clark et al. (2018). Further processing of the data is discussed in Section 4.

3 DATA REDUCTION PIPELINE FOR *SWIFT* UVOT IMAGES OF EXTENDED SOURCES

Since the *SWIFT* UVOT instrument was designed to detect point sources, the standard data reduction pipeline is not suitable for extended sources. Therefore, we developed a new reduction pipeline that can easily be exploited to reduce the images for a large sample of galaxies. For the first time, we present here and in quite some

[1] http://dustpedia.astro.noa.gr

Table 1. Information about the data set used in our study. Column 1: Filter name. Column 2: Effective wavelength $\lambda_{\rm eff}$. Column 3: Resolution (full width at half maximum, FWHM), taken from Breeveld et al. (2010) for the *SWIFT* bands and from Clark et al. (2018) for all other bands. Column 4: Galactic foreground extinction $A_\lambda/A_{\rm V}$, obtained by convolving the MW extinction curve with the transmission curve of the filter. Column 5: Calibration uncertainty. Column 6: Reference for the calibration uncertainties. Column 7: Typical background noise.

Filter	$\lambda_{\rm eff}$	FWHM (arcsec)	$A_\lambda/A_{\rm V}$	Cal. unc. (per cent)	Ref. cal.	Sky noise (per cent)
GALEX FUV	1528 Å	4.3	2.65 ± 0.02	4.5	(a)	1.2
SWIFT UVW2	1991 Å	2.92	2.67 ± 0.04	2.8	(b)	2.6
SWIFT UVM2	2221 Å	2.45	2.80 ± 0.05	2.8	(b)	2.5
GALEX NUV	2271 Å	5.3	2.63 ± 0.07	2.7	(a)	1.2
SWIFT UVW1	2486 Å	2.37	2.26 ± 0.13	2.8	(b)	3.2
SDSS *u*	3551 Å	1.3	1.59 ± 0.01	1.3	(c)	8.4
SDSS *g*	4686 Å	1.3	1.19 ± 0.02	0.8	(c)	1.2
SDSS *r*	6165 Å	1.3	0.868 ± 0.007	0.8	(c)	1.2
SDSS *i*	7481 Å	1.3	0.649 ± 0.005	0.7	(c)	1.6
SDSS *z*	8931 Å	1.3	0.474 ± 0.003	0.8	(c)	5.2
2MASS *J*	1.24 μm	2.0	0.284 ± 0.003	1.7	(d)	13
2MASS *H*	1.66 μm	2.0	0.181 ± 0.002	1.9	(d)	32
2MASS *Ks*	2.16 μm	2.0	0.118 ± 0.001	1.9	(d)	22
IRAC 3.6	3.6 μm	1.66	0.0528 ± 0.0011	3	(e)	2.8
IRAC 4.5	4.5 μm	1.72	0.0361 ± 0.0010	3	(e)	8.9
IRAC 8.0	8.0 μm	1.98	0.00	3	(e)	9.8
MIPS 24	24 μm	6	0.00	5	(f)	7.6
PACS 70	70 μm	5.8	0.00	7	(g)	22
PACS 100	100 μm	6.9	0.00	7	(g)	16

Note. References calibration uncertainties: (a) Morrissey et al. (2007). (b) Calculated from table 1 of the *SWIFT* UVOT CALDB Release Note 16-R01: https://heasarc.gsfc.nasa.gov/docs/heasarc/caldb/swift/docs/uvot/uvot_caldb_AB_10wa.pdf. (c) SDSS DR12 Data Release Supplement: http://www.sdss.org/dr12/scope/. (d) Cohen et al. (2003). (e) IRAC Instrument Handbook: https://irsa.ipac.caltech.edu/data/SPITZER/docs/irac/iracinstrumenthandbook/17/#_Toc410728305. (f) MIPS Instrument Handbook: https://irsa.ipac.caltech.edu/data/SPITZER/docs/mips/mipsinstrumenthandbook/42/#_Toc288032317. (g) PACS Instrument and Calibration Web Pages: http://herschel.esac.esa.int/twiki/bin/view/Public/PacsCalibrationWeb#Photometer_calibration_in_scan_m.

depth our new pipeline, which will be made publicly available in the future.

Images were retrieved from NASA's HEASARC (High Energy Astrophysics Science Archive Research Center) Archive, using the *SWIFT* Data Query form.[2] UVOT data are taken in three modes: Image mode, Event mode, and Image&Event mode. We only obtained the IMAGE data in the three UV filters: *UVW2*, *UVM2*, and *UVW1*. Our reduction pipeline uses several tasks from the specialized HEASOFT software (version 6.17), which can be downloaded from the HEASARC website.[3] We created PYTHON scripts that perform these tasks in an automatic way to all images so that the pipeline can be applied to other galaxies very easily and efficiently. We furthermore implemented a pixel-by-pixel correction for coincidence loss (i.e. the systematic underestimation of flux when multiple photons arrive simultaneously at the photon counter, see Section 3.4.1). The rest of this section describes the different steps of our pipeline: aspect correction, creation of auxiliary maps, combination of separate frames, several corrections to the flux, combination of different epochs, and calibration and aperture correction.

3.1 Aspect correction

We start from the SKY maps retrieved from the archive. The astrometry of these individual maps is not exact and needs to be corrected for slight offsets. This so-called 'aspect correction' happens in two steps, with the HEASOFT task `uvotskycorr`.[4] In the first step, the aspect corrections are calculated and saved to a file. The task identifies stars in every frame and compares the detected sources with the USNO-B1.0 all-sky catalogue (Monet et al. 2003). A correction is only calculated if at least three detected sources can be matched to sources in the catalogue. An aspect correction could not be found for all frames. This can be the case, e.g. when there are not many (bright) stars in the field of view with a high enough signal-to-noise ratio (SNR). However, in our case, an aspect correction was found for most of the images. The other images are left out from further analysis. Subsequently, the aspect corrections are applied to the individual frames. The IDs of the images that were eventually used in the analysis are listed in Table A1 in Appendix A. Note that each of these 'images' has several individual frames that need to be reduced separately.

3.2 Creation of auxiliary maps

At this point, three auxiliary maps must be created, which are needed in further steps of the reduction pipeline:

(a) Quality maps:
Quality maps contain flags associated with the goodness or badness of each detector pixel and are used to build exposure maps (see the next step). We create quality maps for each image frame with the task `uvotbadpix`.

[2] https://heasarc.gsfc.nasa.gov/cgi-bin/W3Browse/swift.pl
[3] https://heasarc.nasa.gov/lheasoft/download.html

[4] All tasks in `typewriter` font are HEASOFT tasks, which will not explicitly be repeated in the remainder of the paper.

(b) Exposure maps:
We generate exposure maps based on the aspect-corrected frames and the created bad pixel masks with the task `uvotexpmap`. The exposure maps are used to normalize the frames in a later step (see Section 3.3).

(c) Large-scale sensitivity maps:
Large-scale sensitivity (lss) maps are created for every image frame with the task `uvotskylss` and are used in a later step to correct for the non-uniform sensitivity of the detector (see Section 3.4.2).

3.3 Combination of separate frames and normalization

In order to improve the SNR, the different sky frames should be combined. To co-add the frames, it is important that they are perfectly aligned, i.e. that the aspect correction was calculated and applied correctly to each frame. Furthermore, at this stage, we can only add images that were observed more or less during the same period. Because the UVOT detectors suffer from sensitivity loss over the years, we need to correct for this in a later step (see Section 3.4.3). The later the images were taken, the larger this correction will be, so we need to separate images taken in different periods. In our case, we ended up with four summed images, one for each of the four years in which NGC 628 was observed: 2007, 2008, 2013, and 2015. It is important to note that in this step we also sum the exposure maps and the lss maps. With the `ftappend` task, all frames are first appended into one single image, and with `uvotimsum` the different frames are then actually summed.

Subsequently, we normalize the total sky images so that the units are converted from counts to count rates (i.e. counts s^{-1}). This is required for the calculation of the correction factors in the following step (Section 3.4). Hereto, we divide the summed sky images by their corresponding summed exposure maps, using the task `farith`.

3.4 Flux corrections

3.4.1 Coincidence loss correction

In the photon-counting detector employed in the UVOT, the incoming signal from each individual photon generates a splash of photons across multiple pixels on the CCD camera, with the centre of the splash giving positional information accurate to a sub-CCD-pixel scale for point sources. The detector has a readout speed (or frame time) of about 11 ms in full-frame imaging mode (Roming et al. 2005), which may lead to a systematic underestimation of photon energy (so-called 'coincidence loss' or 'pile-up') when two or more photons arrive at a similar location on the detector within the same CCD readout interval. The detector is not sensitive above a certain photon count rate. Thus, for extended sources with higher count rates of incoming photons, it can happen that the simultaneous arrival of multiple photons is counted as one single photon, and/or that the detection of the incoming photons is misplaced by the centroiding algorithm.

We need to correct for this coincidence loss to recover the true incoming photon rate. Based on a detailed analysis of the UVOT response to different background models in Breeveld et al. (2010), the coincidence loss correction has been shown to become non-negligible for regions with count rates higher than 0.007 counts s^{-1} $pixel^{-1}$ for an unbinned pixel grid (with a pixel size 0.5 arcsec × 0.5 arcsec). We use 2 × 2 binned images (with a pixel size 1 arcsec × 1 arcsec), so the critical count rate is 0.028 counts s^{-1} $pixel^{-1}$. In Fig. 2, we indicate the regions with a higher count rate in the co-added *UVW1* image from 2015. Particularly in the spiral arms and the star-forming regions of NGC 628, this threshold is easily exceeded, so a coincidence loss correction becomes inevitable.

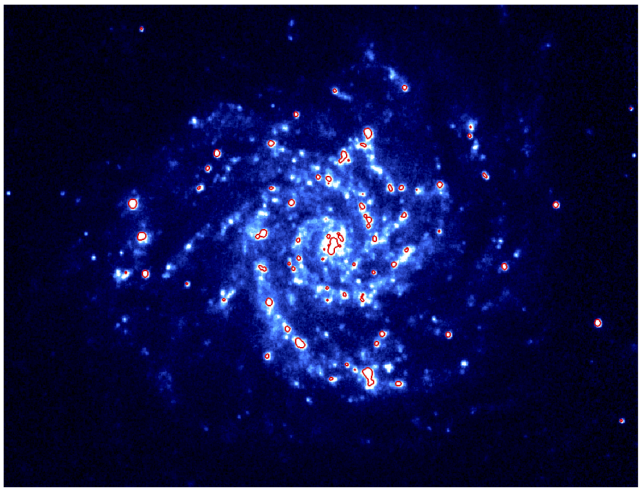

Figure 2. Co-added *SWIFT UVW1* image from 2015 with contours indicating the regions with a count rate higher than 0.028 counts s^{-1} $pixel^{-1}$, for which the coincidence loss becomes significant.

Since the UVOT instrument was mainly designed to observe gamma-ray bursts and other high-energy sources, the existing calculations of coincidence loss corrections have been optimized for point sources. The correction factor is standardly derived from an aperture with a 5 arcsec radius around the point source. This choice of aperture size (with a radius of 5 arcsec) is driven by its minimal contribution from tails of the point spread function (PSF; Poole et al. 2008). The default procedure is not applicable to sources of angular extent larger than the size of the standard 5 arcsec aperture. Karczewski et al. (2013) present a method to correct for coincidence loss in extended sources in which they divide the galaxy image into regions of similar count rates, following isophotal contours. The coincidence loss correction factors are determined from representative 5 arcsec 'test' apertures and applied to correct photon count rates in the corresponding regions. In Hoversten et al. (2011), the resolved regions in M81, where coincidence loss corrections were required, were limited, and point-source corrections could be applied to a couple of individual regions. This approach is, however, not feasible for pixel-by-pixel studies. Therefore, we had to come up with a new strategy to calculate and apply coincidence loss corrections to extended sources. We adapted the correction technique for point sources of Poole et al. (2008) to a pixel-by-pixel algorithm. Because of the photon splash that is created in the detector, one cannot simply calculate a correction factor for each individual pixel without taking into account the surrounding pixels. Therefore, we determine the coincidence loss correction factor within a 9 × 9 pixel sized box (or 81 $arcsec^2$ in our case) centred on the pixel of interest, which covers an area equivalent to an $R = 5$ arcsec aperture region. The coincidence-loss-corrected count rate $C_{\rm coicorr}$ (in counts s^{-1}) in a certain pixel is calculated as

$$C_{\rm coicorr} = C_{\rm obs} \times f_{\rm coicorr}, \quad (1)$$

where $C_{\rm obs}$ is the observed count rate in that pixel and $f_{\rm coicorr}$ is the coincidence loss correction factor determined within a 9 × 9 pixel sized box centred on that pixel. The detailed calculation of

this correction and of the uncertainty on the corrected flux can be found in Appendix B.

It must be mentioned at this point that our sliding-box correction method has its limitations. For very high flux rates (and thus large coincidence losses), the area around the star (or bright source) becomes dark because of the displacement of counts that was discussed earlier, which cannot be fixed with our method. Furthermore, when calculating the correction factor in a box that is larger than the source, the correction can be underestimated in the central regions of a bright source and overestimated around the bright region. However, in our case the typical coincidence loss corrections are relatively small compared to the overall uncertainties on the *SWIFT* fluxes (4.5–6 per cent on average). For the relevant regions (with pixel values exceeding the critical count rate of 0.028 counts s^{-1} $pixel^{-1}$), we find corrections between 0.5 and 3 per cent, with larger corrections only encountered in regions that were later masked as foreground stars. Moreover, since the images are rebinned in a later stage (see Section 4) to pixels that are 7 times bigger, possible local over and/or undercorrections are averaged out.

3.4.2 *Large-scale sensitivity correction*

As explained before, the lss correction accounts for the non-uniform sensitivity of the detector (i.e. the sensitivity varies with large-scale changes of position on the detector). This step resembles the standard flat-fielding correction that is carried out for CCD cameras, but since a photon-counting instrument is insensitive to low-level CCD throughput variations, a traditional flat-field correction is not appropriate. For the details of the calculation of this correction, we refer the reader to section 5 of Breeveld et al. (2010). The correction can be applied by dividing the coincidence-loss-corrected map by its corresponding lss map that was created earlier, using the `farith` task.

3.4.3 *Zero-point correction*

As mentioned before, the sensitivity of the detector decreases over the course of several years since the beginning of the *SWIFT* mission in 2005 January. We need to correct for this sensitivity loss by applying a zero-point correction ($f_{\rm zpcorr}$), which can be calculated with the following quadratic function (from the *SWIFT* UVOT CALDB Release Note 15-03[5]):

$$f_{\rm zpcorr} = at^2 + bt + c \tag{2}$$

with t the time in years after 2005 January 1 and the parameters a, b, and c taken from table 3 of the same Release Note[5]. Typical corrections are found to be between 1 and 20 per cent depending on the filter and the year in which the image was taken. The zero-point-corrected count rate $C_{\rm zpcorr}$ (in counts s^{-1}) can then be calculated as

$$C_{\rm zpcorr} = \frac{C_{\rm coicorr}}{f_{\rm zpcorr}}. \tag{3}$$

The uncertainty on this correction is included in the total calibration uncertainty listed in Table 1.

[5] https://heasarc.gsfc.nasa.gov/docs/heasarc/caldb/swift/docs/uvot/uvotcaldb_throughput_03.pdf

3.5 Combination of the different epochs

Now that all corrections have been applied to the images, the four different summed images (from different years) can be combined. We therefore convert the units of the images from count rates back to the original counts, sum the images (and their corresponding exposure maps), and afterwards normalize the total image again by dividing by the total exposure map.

3.6 Calibration and aperture correction

In a final step, we convert the units of the combined image from count rates $C_{\rm tot}$ (in counts s^{-1}) to flux densities (Jy):

$$F({\rm Jy}) = C_{\rm tot} \times f_{\rm cal} \times 10^{23} \tag{4}$$

using the calibration factors $f_{\rm cal}$ listed in the first column of table 2 of the *SWIFT* UVOT CALDB Release Note 16-R01.[6]

It is very important at this point to realize that these calibration factors were determined based on apertures with a 5 arcsec radius, which only contain approximately 85 per cent of the total flux of a point source (Breeveld et al. 2010). Therefore, the calibration factors have been upscaled in such a way that using these factors in a 5 arcsec aperture around a point source results in the correct flux for that source. However, if we would use these factors directly to calibrate the flux in every individual pixel in the image, we would overestimate the flux. Therefore, we need to compensate for this by using the curve of growth (see fig. 1 of Breeveld et al. 2010), which reaches a plateau for an aperture with a radius of about 30 arcsec. The total encircled energy in this 'maximum' aperture, normalized to the encircled energy in a 5 arcsec aperture is exactly the aperture correction $f_{\rm apcorr}$ that was applied to the calibration factors. To obtain the true pixel fluxes, we thus need to downscale them again:

$$F_{\rm corr}({\rm Jy}) = F({\rm Jy}) / f_{\rm apcorr} \tag{5}$$

(with $f_{\rm apcorr}$ = 1.1279, 1.1777, and 1.1567 for the *UVW2*, *UVM2*, and *UVW1* filters, respectively). The final reduced images in the three filters were combined into a colour image, shown in Fig. 3.

4 DATA PROCESSING WITH PTS

Further processing of the *SWIFT* images, as well as of all other waveband images (*GALEX FUV*/*NUV*, SDSS *u*/*g*/*r*/*i*/*z*, 2MASS *J*/*H*/*Ks*, IRAC 3.6/4.5/8.0 μm, MIPS 24 μm, and PACS 70/100 μm), is done by means of PTS[7] (a PYTHON toolkit for SKIRT), developed by Verstocken et al. (in preparation). This toolkit is designed to post-process SKIRT radiative transfer simulations (Baes et al. 2003, 2011; Camps & Baes 2015), but also to prepare images for SKIRT and for other purposes. The image processing includes subtraction of foreground stars/objects, correction for Galactic extinction, convolution, rebinning, background sky subtraction, and uncertainty calculation. The code has been automated in such a way that it can be used for different images with very little manual intervention.

The removal of the foreground objects is performed in two steps. First, PTS searches in the 2MASS All-Sky Catalogue of Point Sources II/246 (Skrutskie et al. 2006) for stars and in the HyperLeda[8] I Catalogue VII/237 (Makarov et al. 2014) for galaxies

[6] https://heasarc.gsfc.nasa.gov/docs/heasarc/caldb/swift/docs/uvot/uvot_caldb_AB_10wa.pdf
[7] http://www.skirt.ugent.be/pts/
[8] http://leda.univ-lyon1.fr/

Table 2. Bump and slope values obtained with CIGALE for pixel 261 258 and median values for NGC 628 for the 'standard' case explained in Section 6.1, and for the different tests described in Section 6.3: leaving out the *SWIFT* fluxes, changing the SFH, adding differential reddening, and fitting the global SED.

Parameter	Pix 261 258	NGC 628∗	No *SWIFT*∗	SFH2EXP∗	Diff. red.∗	NGC 628 global
B	0.85 ± 0.48	2.31 ± 0.95	2.05 ± 1.15	2.93 ± 1.08	1.87 ± 0.91	2.24 ± 1.16
δ	-0.47 ± 0.07	-0.37 ± 0.10	-0.32 ± 0.10	-0.35 ± 0.12	-0.19 ± 0.10	-0.55 ± 0.15

Note. $^*A_V > 0.2$.

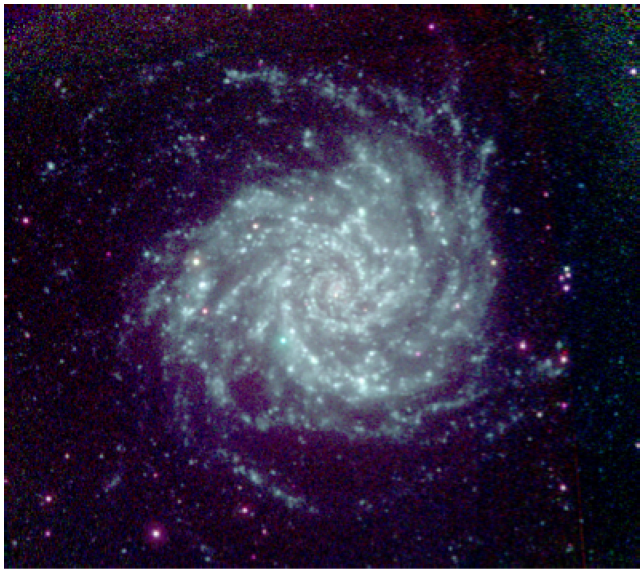

Figure 3. Colour image created by combining the three final reduced UV *SWIFT* images: *UVW2* in blue, *UVM2* in green, and *UVW1* in red.

within the field of view of the image and tries to link these to actual sources in the image. Apart from stars and galaxies, the procedure will also detect other flux sources that do not belong to the target. In the second step, all detected sources are 'removed'. The pixel values in the detected regions are replaced by average local background values, determined by fitting a polynomial to the surrounding pixels and imposing a representative pixel-to-pixel noise variation, based on the standard deviation of the fitting. This approach ensures that the foreground objects are replaced by pixel values as close as possible to the (galaxy) emission in that particular region. When convolving the image in a later step, this results in a more realistic effect of those pixels on the surrounding areas, compared to when the pixels are simply masked. However, it must be noted that those 'artificial' pixels were eventually excluded from the analysis [colour plots and spectral energy distribution (SED) fitting] in order to make sure we only use genuine measured fluxes.

Since we are interested in the attenuation properties of the dust in NGC 628, we must correct for the extinction caused by dust in the MW. The MW extinction in the (CTIO) *V*-band for NGC 628 is determined at $A_V = 0.188$ (obtained from the IRSA Galactic Dust Reddening and Extinction Archive[9]). Because this archive lacks extinction measurements in the *GALEX* and *SWIFT* bands, we convolve the MW extinction curve (Cardelli et al. 1989) with the transmission curves of all filters, taken from the SVO Filter Profile Service.[10] The obtained Galactic foreground extinction A_λ/A_V in all filters is given in Table 1. It should be noted that, in fact, this method will only give the correct MW extinction value if the background source has a flat response curve within every passband, which is of course not exactly true. We verified the effect of a non-flat spectrum by extinguishing the SED of the unattenuated stellar emission in NGC 628 obtained with CIGALE (see Section 6) with the MW extinction curve. Comparing the attenuated and the unattenuated fluxes in every band results in the 'real' MW extinction correction factors for all filters. The maximum differences between the correction factors found in this way and the average values that were used to correct the images for MW extinction (reported in Table 1) were added to the same table as an upper estimate of the uncertainty on the correction factors, and are negligible compared to the other uncertainties.

We convolve all images to the poorest resolution in our data set, i.e. that of the PACS 100 μm image, which has a PSF with an FWHM of 6.9 arcsec. We use the new 2018 Aniano kernels (Aniano et al. 2011),[11] which are rebinned to the same pixel grid as the image, normalized and aligned by PTS. In view of performing a pixel-by-pixel analysis, we rebin all images to a common pixel grid with a pixel size of 7 arcsec × 7 arcsec, which is approximately equivalent to the resolution of the convolved images. In this way, the vast majority of the PSF is concentrated in a single pixel (Bendo et al. 2012, 2015; Viaene et al. 2014). The physical size of each pixel is about 325 pc.

Finally, the background emission needs to be subtracted from each image. We determine the sky background by randomly placing several apertures (typically about 100) with a radius of 4 times the FHWM of the PSF (about 28 arcsec in our case) in 'empty' parts of the image where no sources were removed. The sky background is then estimated as the median of the mean flux densities in all these apertures, and is subtracted from the image.

For further analysis and for the SED fitting (Section 6), it is important to have an estimate of the uncertainties on the flux densities in every pixel of every image. There are several factors of uncertainty that need to be taken into account:

(i) Large-scale variation in the background: This is computed as the standard deviation of the mean background values that were derived in the different apertures.

(ii) Pixel-by-pixel variation in the background: This is computed as the mean value of the standard deviations of the pixel values in the different background apertures. The total background noise (i.e. the square root of the quadratic sum of the large- and small-scale variations) in every image is given in Table 1.

[9] https://irsa.ipac.caltech.edu/workspace/TMP_9ckowT_16010/DUST/NGC628.v0001/extinction.html

[10] http://svo2.cab.inta-csic.es/svo/theory/fps3/

[11] https://www.astro.princeton.edu/ ganiano/Kernels/

(iii) Calibration uncertainty: This is the uncertainty on the calibration of the instruments based on standard sources. Values are listed in Table 1.

(iv) Poisson noise: This accounts for the particle properties of light and the fact that the rate at which photons arrive at the detector is not exactly the same at every moment in time. The photons emitted at shorter wavelengths are less numerous, and therefore, the UV images will be more affected by this photon noise or Poisson noise. For this reason, we only calculate the Poisson noise for the *GALEX* and *SWIFT* images, starting from the original images in units of counts: Poisson noise $= \sqrt{N}$ with N the number of photons.[12]

PTS calculates these uncertainties and sums them quadratically (in every pixel) to compute a total uncertainty map on the flux densities.

As a final quality check of the *SWIFT* data, we compare the global galaxy flux in the *SWIFT UVM2* and *GALEX NUV* bands, because these filters are centred around the same wavelengths. From the images, we find a global flux of $(8.13 \pm 0.28) \times 10^{-2}$ Jy in the *UVM2* band and of $(8.32 \pm 0.24) \times 10^{-2}$ Jy in the *NUV* band. These values are fully consistent, given the different filter properties.

5 UV COLOUR–COLOUR PLOTS

A first analysis of the UV data can be done through colour–colour plots, as given in Fig. 4. They are a first step to compare models with observations and inform us about the stellar population and the level of attenuation in the galaxy. The dots represent the different pixels in the galaxy image with an SNR>5 in the five UV bands (resulting in 5051 data points), whereas the lines are theoretical curves obtained by attenuating the spectra of single stellar populations (SSPs) assuming different levels of dust attenuation and different dust extinction and attenuation laws (all shown in Fig. 8): the Calzetti et al. (2000) attenuation law (dashed lines), the MW extinction law from Cardelli et al. (1989) with $R_V = 3.1$ (solid lines), the SMC extinction curve from Gordon et al. (2003) (dotted lines), and the median attenuation curve for NGC 628 that we obtained from the CIGALE fitting (see Section 6.2; dash–dotted lines). The SSPs are taken from the library of Bruzual & Charlot (2003) with a Chabrier (2003) initial mass function, assuming a solar metallicity ($Z = 0.02$) (and are also used in the modelling in Section 6). The different lines correspond to SSPs with different ages (10 Myr in blue, 100 Myr in green, and 300 Myr in magenta). As we are looking at UV colours, we expect the light to be dominated by young stars of a few 100 Myr or younger, which is indeed confirmed by the data points in the plots. As will be explained at the end of this section, galaxies are generally better characterized by continuous-age rather than single-age populations. Therefore, we also added models (in black) for a stellar spectrum obtained by combining SSPs of different ages, assuming a constant SFR. In addition, some V-band attenuation levels are indicated ($A_V = 0.0$ with circles, 0.5 with triangles, 1.0 with diamonds, 1.5 with squares, and 2.0 with stars). Most regions in NGC 628 seem to be consistent with an A_V between 0 and 1.5. Finally, we colour coded the data points according to the empirically derived sSFR in the corresponding pixel. It is clear that regions in the galaxy with higher sSFR exhibit younger stars, as expected.

The scatter plots compare four different UV colours: *UVW2−UVM2*, *UVM2−UVW1*, *FUV−NUV*, and *UVW2−UVW1*. The *UVW2−UVW1* and *FUV−NUV* colours are most sensitive to the UV slope of the attenuation curve, with the largest values for the *FUV−NUV* colour (at fixed stellar age and V-band attenuation A_V) observed for the steep SMC curve. Furthermore, there is a dependence on the bump strength (in the *NUV* band), which is reflected in smaller *FUV−NUV* colours for MW curves (which have a bump feature) compared to (bumpless) Calzetti curves, even though the UV slope (without bump) is steeper for the MW compared to the Calzetti law. Finally, the *FUV−NUV* colour also depends on the stellar age, especially for an MW-type dust extinction curve with a shallow UV slope, with larger values for older stellar populations. The *UVW2−UVW1* colour probes the shape of the UV slope on opposite sides of the 2175 Å bump feature. Again, the largest values are obtained for the steepest curve (SMC) (at fixed stellar age and A_V). Most of the data points (for spatially resolved regions in NGC 628) show a linear correlation in the *FUV−NUV* versus *UVW2−UVW1* diagram (see the bottom left panel), following the trend of the median NGC 628 curve. The theoretical models extincted with an MW curve are much flatter in this diagram (with almost constant *FUV−NUV* for a fixed stellar age), inconsistent with the observed trend for the resolved regions in NGC 628, suggesting that the dust law in this galaxy is generally steeper than the MW curve (and/or has a less prominent bump feature).

The colours *UVW2−UVM2* and *UVM2−UVW1* are more sensitive to the bump feature with the *UVM2* band coinciding with the position of the 2175 Å bump feature (see Fig. 1). Due to the longer tails of the *UVW2* and *UVW1* transmission curves, these colours do not perfectly measure the bump strength relative to the continuum at those wavelengths. The majority of resolved regions in NGC 628 have a negative *UVW2−UVM2* colour, implying that the observed *UVM2* flux is lower than the *UVW2* flux. Similarly, the positive *UVM2−UVW1* colours imply that $\text{flux}_{UVM2} < \text{flux}_{UVW1}$. This dip in the flux around 2200 Å indeed suggests the presence of a bump feature in the attenuation curve around this wavelength. The scatter in the plots with *UVW2−UVM2* colours (i.e. the top left and middle column panels) is dominated by the uncertainties on the *SWIFT* fluxes (over the limited dynamic wavelength range covered in *UVW2−UVM2* colours), and does not help us much to distinguish between various theoretical models. Nevertheless, the data points in these plots seem to be covered mostly by an MW-type extinction curve, again a hint for a prominent bump feature. Likewise, the observed *UVM2−UVW1* colours (in the bottom right and the middle row panels) can only be recovered by theoretical models assuming an MW-like bump strength (or a bump strength similar to the median NGC 628 curve), also suggesting a relatively strong bump (within the error bars) for most regions in NGC 628. The fact that most of the data points in the bottom right plot show a linear correlation following the trends of the steeper curves suggests that a flat UV slope, as in the MW curve, is not adequate to reproduce the data, and that a steeper slope is required (at least in a large part of the galaxy). Finally, the strongest correlation is observed in the *UVM2−UVW1* versus *UVW2−UVW1* colour diagram. Due to the limited wavelength range probed in the colours on both the axes of this plot, it is mostly sensitive to the bump strength (and not so much to the UV slope). The data points clearly coincide with the MW curves, meaning that a prominent bump feature must be present in the attenuation curve of NGC 628.

[12] As described in Kuin & Rosen (2008), the uncertainty on the *SWIFT* measurements, in fact, does not follow a Poisson distribution but a binomial distribution due to the coincidence loss of the detector. However, for low count rates (<0.05 counts/frame) the difference is negligible, as can be seen in their fig. 1. Since the highest measured count rate in our images is 0.02 counts/frame, there will be no effect on the uncertainties.

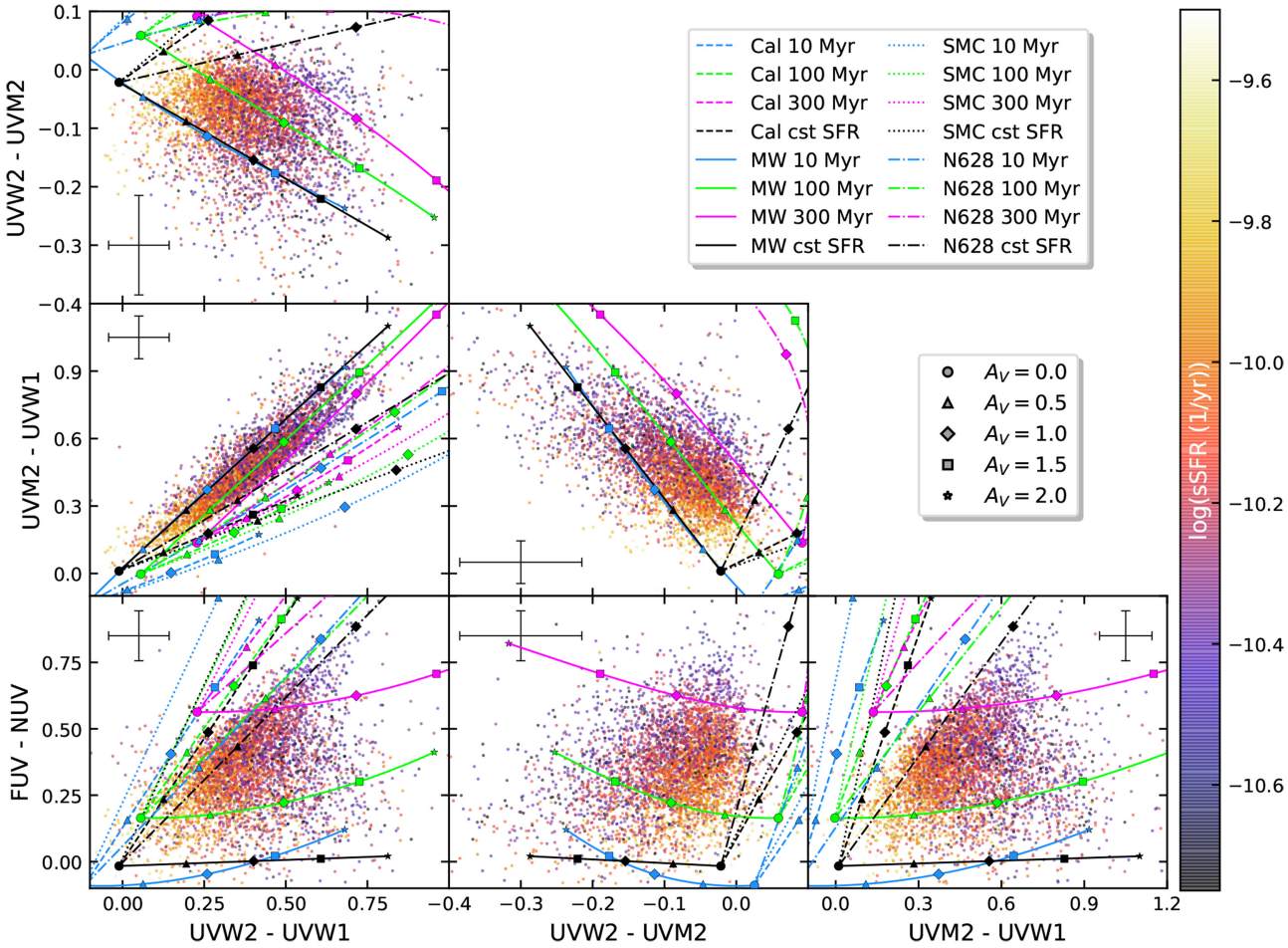

Figure 4. UV colour–colour plots. The dots represent the different pixels in NGC 628 (5051 data points), whereas the lines are theoretical curves obtained by attenuating the spectra of SSPs (and a combined spectrum) with different levels of dust attenuation and different dust extinction and attenuation laws: the Calzetti et al. (2000) attenuation law (dashed), the MW extinction law from Cardelli et al. (1989) with $R_V = 3.1$ (solid), the SMC extinction curve from Gordon et al. (2003) (dotted), and the median attenuation curve for NGC 628 that we obtained from the CIGALE fitting (dash–dotted). A median error bar on the data points is shown. Some *V*-band attenuation levels are indicated ($A_V = 0.0$ with circles, 0.5 with triangles, 1.0 with diamonds 1.5 with squares, and 2.0 with stars). The data points are colour coded according to their sSFR. (The stellar mass is derived from the IRAC 3.6 μm image after correction for dust emission, while the SFR is derived from the *FUV* image, corrected for dust extinction.)

An important note to make here is that stars have been forming throughout a galaxy's lifetime, and usually do not form during a single burst of star formation. Therefore, in addition to simple single-age SSPs, we have also overlaid theoretical curves assuming a constant SFR (in black). In the most constraining colour diagrams (middle left, bottom left, and bottom right panels), these curves agree relatively well with the observed colours (especially for the median NGC 628 curve), indicating that this continuous age model is more adequate than the single-age SSPs to represent the resolved stellar populations in this galaxy. In summary, the colour plots suggest that the resolved regions in NGC 628 are consistent with a UV slope steepness in between the MW and SMC dust extinction curves, and are best fitted with an MW-type bump strength. However, we need to be careful with our conclusions as the theoretical curves in these plots only represent a limited number of stellar ages, SFHs, and dust attenuation curve shapes. Moreover, we are subject to degeneracies between the age of the stellar populations, the attenuation level, and the shape of the attenuation curve, which cannot be ruled out from these simple colour–colour plots. Therefore, in the second part of this work, we perform a more accurate modelling of the underlying stellar population, and allow for more flexibility in the parameters describing the dust attenuation curve, using the SED fitting code CIGALE.

6 MODELLING DUST ATTENUATION WITH CIGALE

6.1 Description and method

In order to constrain the dust attenuation curve on resolved scales in NGC 628, we use CIGALE[13] (a PYTHON Code Investigating GALaxy Emission, Noll et al. 2009; Roehlly et al. 2014; Boquien et al. 2018) to fit an SED to our multiwavelength data set. CIGALE can model the FUV to radio spectrum of galaxies and estimate their physical

[13] https://cigale.lam.fr/

properties such as the SFR and SFH, the attenuation by dust, the dust luminosity and mass, the stellar mass, and many other physical quantities. The code relies on the dust energy balance principle: the energy that is emitted by dust in the IR matches the energy that was absorbed by dust in the UV–optical range. It uses a combination of several SSPs, SFHs, and a flexible attenuation curve. A large grid of models is fitted to the data and the physical properties are determined through the analysis of the likelihood distribution. This is based on Bayesian statistics, in which the physical properties are estimated by weighting the models depending on their goodness of fit. This method also directly returns the uncertainties on the estimated quantities. CIGALE has been used extensively in a broad range of studies, such as the IRX–β relation (Boquien et al. 2012), attenuation properties of galaxies (Buat et al. 2011, 2012; Boquien et al. 2013; Lo Faro et al. 2017), SFR estimators (Boquien, Buat & Perret 2014; Buat et al. 2014; Boquien et al. 2016), and so on.

We use CIGALE to fit an SED for every individual pixel in NGC 628 to the following bands: *GALEX FUV*/*NUV*, *SWIFT UVW2*/*UVM2*/*UVW1*, SDSS *u*/*g*/*r*/*i*/*z*, 2MASS *J*/*H*/*Ks*, and IRAC 3.6 μm/4.5 μm. In addition, we use the total infrared (TIR) luminosity in every pixel as an extra data point in the fitting (see later). We only fit those pixels with a sufficiently high SNR (>3) in all bands (3530 pixels in total). Since our main goal is to constrain the attenuation curve (and not the full SED), we want to limit the N-dimensional parameter space in the fitting as much as possible. Therefore, we restrict ourselves to the UV–optical–NIR wavelength range and solely estimate the dust attenuation properties and SFH. Dust emission can be represented by a simple fixed model as explained below. Going beyond the IRAC 4.5 μm band would complicate the situation, and would require to fit dust emission templates, significantly increasing the number of SED models to be considered in the fitting. Finally, since the FIR images beyond 100 μm have a poorer resolution, we would not be able to do the fitting on resolved scales of 7 arcsec.

To avoid degeneracies between the age of stellar populations and the level of dust attenuation, which could potentially bias the inference of the dust attenuation curve parameters, we compensate the 'lack' of FIR fluxes by adding the total dust luminosity as an extra constraint to the models, calculated in every pixel as prescribed by Galametz et al. (2013) (see their table 3):

$$S_{\mathrm{TIR}} = 2.162 \times S_{24} + 0.185 \times S_{70} + 1.319 \times S_{100} \quad (6)$$

with S_{TIR} the TIR luminosity density in units of W kpc^{-2}, and S_{24}, S_{70}, and S_{100} the luminosity density in the MIPS 24 μm, PACS 70 μm, and PACS 100 μm bands, respectively. Poggianti, Bressan & Franceschini (2001) already used the total FIR as a constraint to model star formation and dust extinction in luminous starburst galaxies. This approach of fitting the UV/optical SED and including constraints on the dust emission directly from the TIR luminosity, referred to as IR luminosity-constrained SED fitting (SED + LIR fitting), is also used by and described in Salim et al. (2018). In this way, the IR luminosity is treated as another SED 'flux' point that directly constrains the SFR and the attenuation curve without fitting the shape of the IR SED, which significantly reduces the N-dimensional parameter space and consequently the computing time.

Important physical components and processes that are included in the models are the SFH, the stellar photospheric emission, the nebular emission (including continuum and recombination lines) and the dust attenuation and emission. For the SFH, we use the SFHDELAYEDFLEX module (Ciesla, Elbaz & Fensch 2017), which takes into account that the star formation did not start suddenly but more gradually, and which allows for a recent enhancement or decline of the SFR. For the stellar spectrum the module BC03 is adopted, which is built on the SSP library of Bruzual & Charlot (2003), with a Chabrier (2003) initial mass function and assuming a solar metallicity ($Z = 0.02$). The same SSPs were used in the empirical colour analysis in Section 5. The nebular emission is modelled based on nebular templates from Inoue (2011). For the dust attenuation, we use the DUSTATT_CALZLEIT module that is based on the Calzetti et al. (2000) starburst attenuation curve. The global slope of the curve can be modified by multiplying it by a power-law function $A(\lambda) \propto \lambda^{\delta}$, and the UV bump is modelled as a Lorentzian-like Drude profile described by three parameters: its central wavelength (which is kept fixed at 2175 Å), its width (or FWHM, fixed at 350 Å), and its amplitude B. In this parametrization, a Calzetti et al. (2000) curve corresponds to $\delta = 0$ and $B = 0$, while the MW extinction curve is approximately equivalent with $\delta \approx -0.15$ and $B = 3$. It is important to note that all stellar populations are attenuated with the same law and same amount of attenuation, so there is no differential reddening between younger and older stellar populations. This is, of course, a simplification as a differential (age-dependent) extinction will lead to changes in the effective (observed) attenuation law due to the fact that young stars suffer a higher attenuation than older stars since they are still enshrouded in their birth clouds (Charlot & Fall 2000; Panuzzo et al. 2007). The effect of this assumption on the results will be verified in Section 6.3. Also the nebular emission lines are attenuated with the same curve. Finally, the dust emission is modelled by the simple DALE2014 module using the dust templates of Dale et al. (2014) (with a fixed slope $\alpha = 2.0$). The parameter values for the SSP library, the nebular emission, and the dust emission are kept fixed, while we let the code fit the parameters of the SFH and the dust attenuation. All parameter ranges used in the fitting are listed in Table C1 in Appendix C. CIGALE makes use of flat priors. Combining all possible parameter values, the code computed and fitted 6 561 000 models to each pixel.

6.2 Fitting results

In Fig. 5, an example of a fitted SED can be found (in this case for pixel 261 258 in the central spiral arm, indicated with a red cross on Fig. 9). We can see that overall the observed data points are fitted very well. This is also true for the other pixels, which is reflected in the residual maps and histograms in Fig. D1 in Appendix D. Residuals mostly lie within the typical uncertainties on the observed flux. We refer the reader to Appendix D for a more detailed discussion on the fitting results in the different wavebands. In Fig. 6, we show the probability distribution functions of some physical properties for pixel 261 258. The slope δ, the FUV attenuation A_{FUV}, and the SFR are constrained reasonably well, while the UV bump amplitude B has a somewhat wider distribution. This is also confirmed by the mock tests described in Appendix E. Table 2 gives the Bayesian bump and slope values obtained for this pixel.

We learn from the histograms in Fig. 7 that there is a large variation in bump strengths and slopes among the different resolved regions in NGC 628. As explained in the previous section, the slope represents the deviation from a Calzetti curve. Negative δ values mean that the curve is steeper than the Calzetti curve. We find a median bump strength of 2.31 with a spread of 1.33 and typical uncertainties around 0.95, and a median slope of −0.37 with a spread of 0.28 and typical uncertainties around 0.10, for regions with a V-band attenuation $A_{\mathrm{V}} > 0.2$ (see Table 2). The

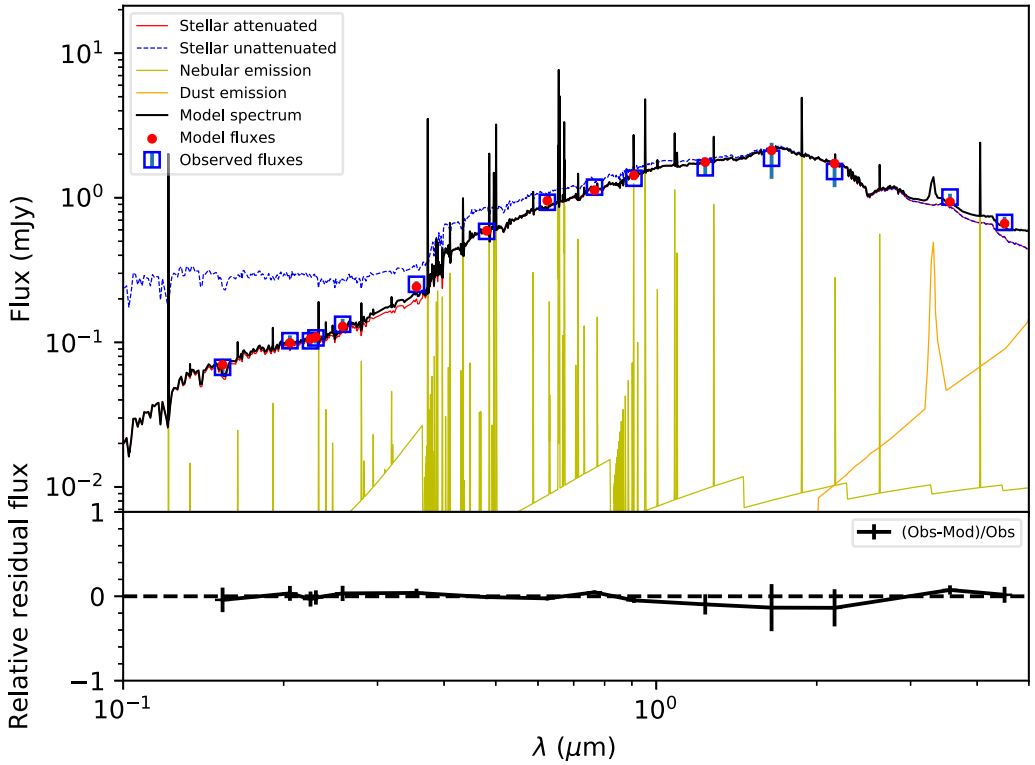

Figure 5. Top: Best-fitting model SED for pixel 261 258 obtained with CIGALE. Bottom: Relative residual flux between model and observations. The observed fluxes are fitted very well (within the error bars).

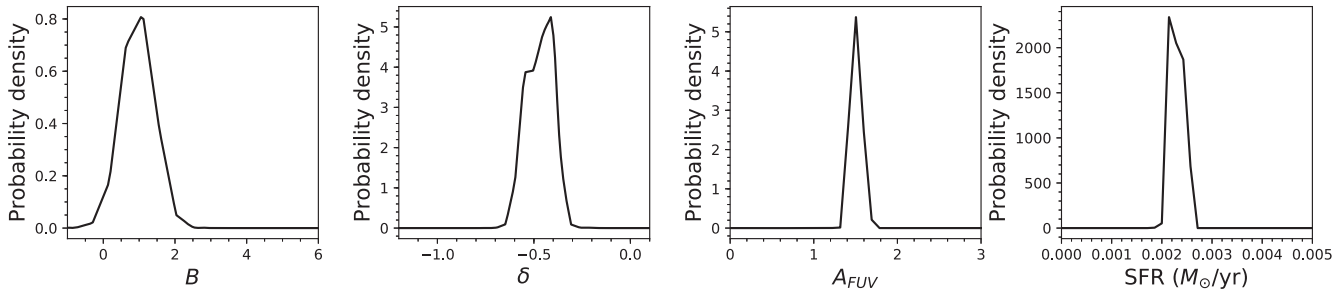

Figure 6. Probability distribution functions of several physical properties obtained with CIGALE for the fit corresponding to pixel 261 258: the UV bump amplitude B, the slope δ, the FUV attenuation $A_{\rm FUV}$, and the SFR are all well constrained.

uncertainties on these parameters are substantial, but from our mock data analyses (described in Appendix E) it is clear that both parameters are constrained reasonably well, especially for regions with $A_{\rm V} > 0.2$. For pixels with a very low dust attenuation, it is more difficult to get meaningful constraints on the attenuation curve. Therefore, in the remainder of this paper we will focus on regions with $A_{\rm V} > 0.2$ because the fitting results are more reliable for these regions.

We plotted our 'median' attenuation curve for NGC 628 (i.e. an attenuation curve with the median bump and slope values stated above, with $A_{\rm V} > 0.2$) in Fig. 8, together with some other relevant curves: the MW extinction curve (from Cardelli et al. 1989), the SMC and LMC extinction curves (from Gordon et al. 2003), the Calzetti et al. (2000) curve, and the average curve for star-forming galaxies with $9.5 < \log(M_*/{\rm M}_\odot) \leq 10.5$ found by Salim et al. (2018) (with $B = 1.73$ and $\delta = -0.3$, see their table 1). The shaded region in the plot represents the attenuation curves between the 16th and 84th percentile of bump and slope values (for $A_{\rm V} > 0.2$ regions). From this, we conclude that the median attenuation curve of NGC 628 has a somewhat shallower slope than the SMC curve ($\delta \approx -0.45$) and a bump that is somewhat smaller compared to the MW curve ($B = 3$). This median curve was also used in the colour plot analysis in Fig. 4.

6.3 Testing of our model

In this section, we verify whether we are able to constrain the attenuation properties with CIGALE and whether the *SWIFT* data aid in this. We also test how our model assumptions on the SFH and the differential reddening affect the modelling output. Finally, we compare the fitting on resolved scales to a fit of the global galaxy SED.

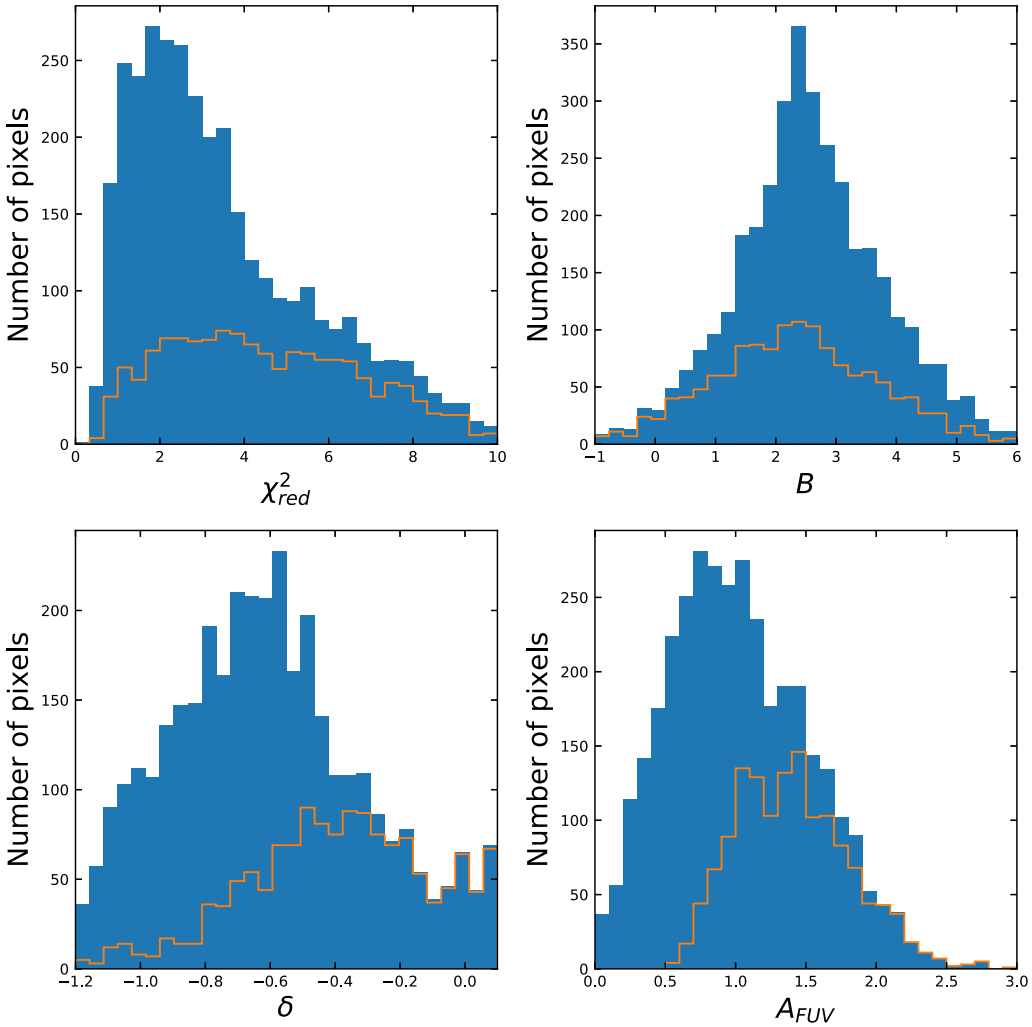

Figure 7. Histograms of the reduced χ^2 of the fitting, the bump strength B, the slope δ, and the FUV attenuation $A_{\rm FUV}$, obtained with CIGALE. We overplot the histogram (in orange) for those pixels with $A_{\rm V} > 0.2$.

In order to prove that our CIGALE model is able to constrain the physical galaxy properties, we performed a mock data analysis. Input data generated from model SEDs for which we know the true parameters are fitted with the same Bayesian approach as before. From this mock testing, we conclude that the model is able to constrain all properties within reasonable uncertainties for regions with a V-band attenuation $A_{\rm V} > 0.2$. For more details on the method and the results of this mock analysis, we refer the reader to Appendix E.

To verify the usefulness of the *SWIFT* bands in constraining the dust attenuation curve, we repeat the exact same fitting procedure, but without the three *SWIFT* fluxes. The results for the median bump and slope, and their uncertainties are in line with the values found before (see Table 2). However, we find that the median relative uncertainty on the bump strength reduces from 56 to 41 per cent when adding the *SWIFT* data. Although it remains hard to constrain the bump feature, the *SWIFT* data clearly assist in this. Since the uncertainties on the *SWIFT* fluxes (4.5–6 per cent on average) are somewhat larger than the *GALEX NUV* uncertainty (around 4 per cent), the *SWIFT* bands are given a smaller weight in the CIGALE fitting compared to the *GALEX NUV*. We found that 'artificially' reducing the *SWIFT* uncertainties so that the *UVM2* uncertainty corresponds to that on the *GALEX NUV* flux further reduces the median relative uncertainty on the bump strength down to 34 per cent (i.e. 22 per cent lower compared to the case without the *SWIFT* data). We thus conclude that when the uncertainties on the *SWIFT* data are lower, they are more helpful in constraining the dust attenuation curve. We expect, for example, that for galaxies with longer exposures (which reduces the Poisson noise) the *SWIFT* data will be even more valuable in constraining the dust attenuation curve on resolved scales.

To check the influence of the SFH assumptions on the results, we did the same modelling as before but this time using the module SFH2EXP. The SFH is parametrized with two decaying exponentials: the first exponential models the long-term star formation, which has formed the bulk of the stellar mass, while the second one models the most recent burst of star formation. The obtained results (see Table 2) are not very different (within the error bars). However, our mock data analysis (see Appendix E) showed that the SFH does have a (limited) influence on the results, especially for regions with lower $A_{\rm V}$. This can indicate that the very steep slope values that we obtained in low-$A_{\rm V}$ (<0.2) regions are possibly biased by the assumptions on the SFH. However, we argue that the delayed and flexible SFH is more adequate to model the resolved regions

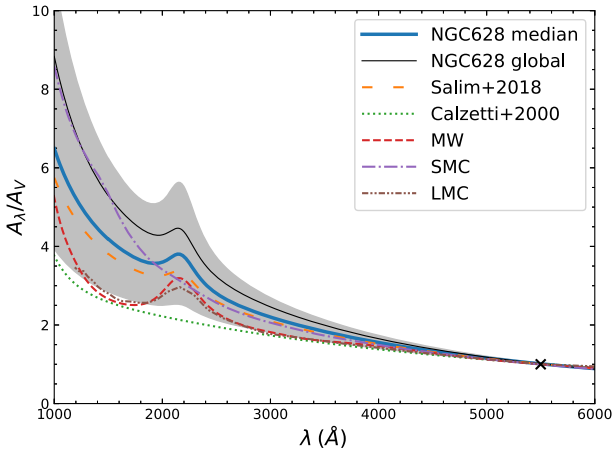

Figure 8. Extinction/attenuation curves for different galaxies. The thick blue line is the median attenuation curve that we obtained for NGC 628 (for $A_V > 0.2$ regions). The region between the 16th and 84th percentile is shaded. The black line is the global attenuation curve of NGC 628. The orange dashed line corresponds to the average attenuation curve from Salim et al. (2018) for star-forming galaxies with $9.5 < \log(M_*/M_\odot) \leq 10.5$ (with $B = 1.73$ and $\delta = -0.3$). The green dotted line is the standard Calzetti et al. (2000) curve. The red dashed line is the average MW extinction curve from Cardelli et al. (1989). Both the SMC (violet dash–dotted) and LMC (brown dash–dot-dotted) extinction curves are taken from Gordon et al. (2003).

in NGC 628 compared to the double exponentially declining SFH. The delayed SFH with a final burst/quench is better adapted because it can more easily represent the more diverse SFHs we expect at a local scale in the galaxy disc: spiral arms had a recent episode of star formation, whereas star formation in interarm regions has fallen. This cannot be obtained with a double exponentially declining SFH. Therefore, we retain the SFHDELAYEDFLEX module.

We also tested whether introducing a differential reddening (i.e. using a different attenuation level for young and old stellar populations due to the extra attenuation for young stars from dust in their birth clouds) changes anything to the results presented in this work. To this aim, we have repeated the modelling of NGC 628 assuming the same dust attenuation curve for young and old stellar populations, but accounting for a different level of dust attenuation, i.e. $E(B-V)_{\rm old} = 0.44\,E(B-V)_{\rm young}$ or $A_{\rm V,\,young}/A_{\rm V,\,old} = 2.27$, consistent with Calzetti et al. (2000), for stars younger than 10 Myr. The median results of this test can be found in Table 2. The bump strength is not very different (within the error bars), but the attenuation curve is shallower. This is to be expected as explained in Salim et al. (2018): the effective attenuation curve (i.e. when 'combining' young and old stars, assuming the same level of attenuation for both populations, as assumed throughout this paper) will be steeper (by $\Delta\delta = -0.2$) than the intrinsic 'individual' curves of the young and old populations (as obtained in this test when using a differential reddening), because the highly attenuated young stars dominate at shorter wavelengths. This is indeed what we observe. However, in the interest of making the simplest assumptions on the geometry and levels of attenuation for different stellar populations, we prefer to use the same level of attenuation for young and old stars.

Finally, we tested whether a fit of the global galaxy SED results in similar attenuation curve parameters as the median values obtained from the pixel-by-pixel fits. We used the same CIGALE set-up as before, but fitting the global fluxes of the galaxy, measured in an aperture that includes all pixels that were fitted before and using the same masks for the foreground stars. The results of this run (see Table 2) are close to the median values from the pixel-by-pixel fitting (within the error bars). Thus, for NGC 628, an investigation of the attenuation curve on resolved scales gives similar results to our finding on a global galaxy scale. This is very promising for our ongoing project (DustKING) studying the global dust attenuation curves of a statistical sample of nearby galaxies (Decleir et al., in preparation, and see Section 7.4). The global attenuation curve of NGC 628 was added to Fig. 8. We also found that this global run significantly benefits from the *SWIFT* data points. Leaving out the *SWIFT* fluxes results in a median relative uncertainty of 124 per cent on the bump strength (which is even consistent with no bump) and 71 per cent on the slope (compared to 52 and 27 per cent when adding the *SWIFT* data, respectively). We thus conclude that the *SWIFT* data are a great added value to constrain the attenuation curve on global galaxy scales.

From the global SED fit of NGC 628, we obtain a total SFR $= 1.30 \pm 0.16\,M_\odot\,{\rm yr}^{-1}$ and a stellar mass of $\log(M_*/M_\odot) = 10.16 \pm 0.04$, which is in reasonable agreement with values found in the literature (SFR $= 1.07\,M_\odot\,{\rm yr}^{-1}$; $\log(M_*/M_\odot) = 9.821$ – Hunt et al. 2018). Salim et al. (2018) studied the dust attenuation curves of 230 000 individual galaxies in the local Universe, in relation to the position of galaxies on the sSFR–M_* diagram. In their fig. 3, NGC 628 is positioned very close to the line of median sSFR for star-forming galaxies in this diagram (i.e. the 'main sequence' of star formation). From this figure, we infer a slope between −0.4 and −0.3 and a bump between 1.0 and 1.5 for galaxies with an sSFR and stellar mass similar to NGC 628. We obtain a global SED with a bump strength that is consistent within the error bars, but a steeper slope, possibly because we are using the same attenuation level for young and old stars, whereas Salim et al. (2018) assume a differential reddening (see the discussion higher up).

7 DISCUSSION OF THE RESULTS

7.1 Resolved stellar and dust parameters

In Fig. 9, we show the distribution of the parameter values obtained with CIGALE across the disc of NGC 628. The stellar mass (M_*) map shows a smooth distribution of the stars, with most stars located in the central regions of the galaxy, and a less pronounced increase in stellar mass surface density in features corresponding to the galaxy's spiral arms. The sSFR map reveals the location of the star-forming regions in the spiral arms of the galaxy. The maps of the bump strength B and the slope δ show the spatial variations of these parameters within the galaxy. Interestingly, we find that the centre of the galaxy is characterized by very steep slopes and strong bumps. However, the V-band attenuation (A_V) map shows little dust in the central region. We argue that the bulge of the galaxy is dominated by older stellar populations and that our assumed attenuation curve (which is based on the Calzetti starburst law) has the property to give low attenuation values in the NIR. In other words, the curve may underestimate dust heating from old stars. CIGALE will try to compensate the 'shortage' of dust emission in the IR with very steep attenuation curves (and thus high $A_{\rm FUV}$ values). Furthermore, the reduced χ^2 values in the central region are relatively high compared to other galaxy regions, which confirms that the central bulge of the galaxy is harder to fit with our model set-up. The interpretation of spatial variations in the bump and slope maps will be further discussed in Section 7.2.

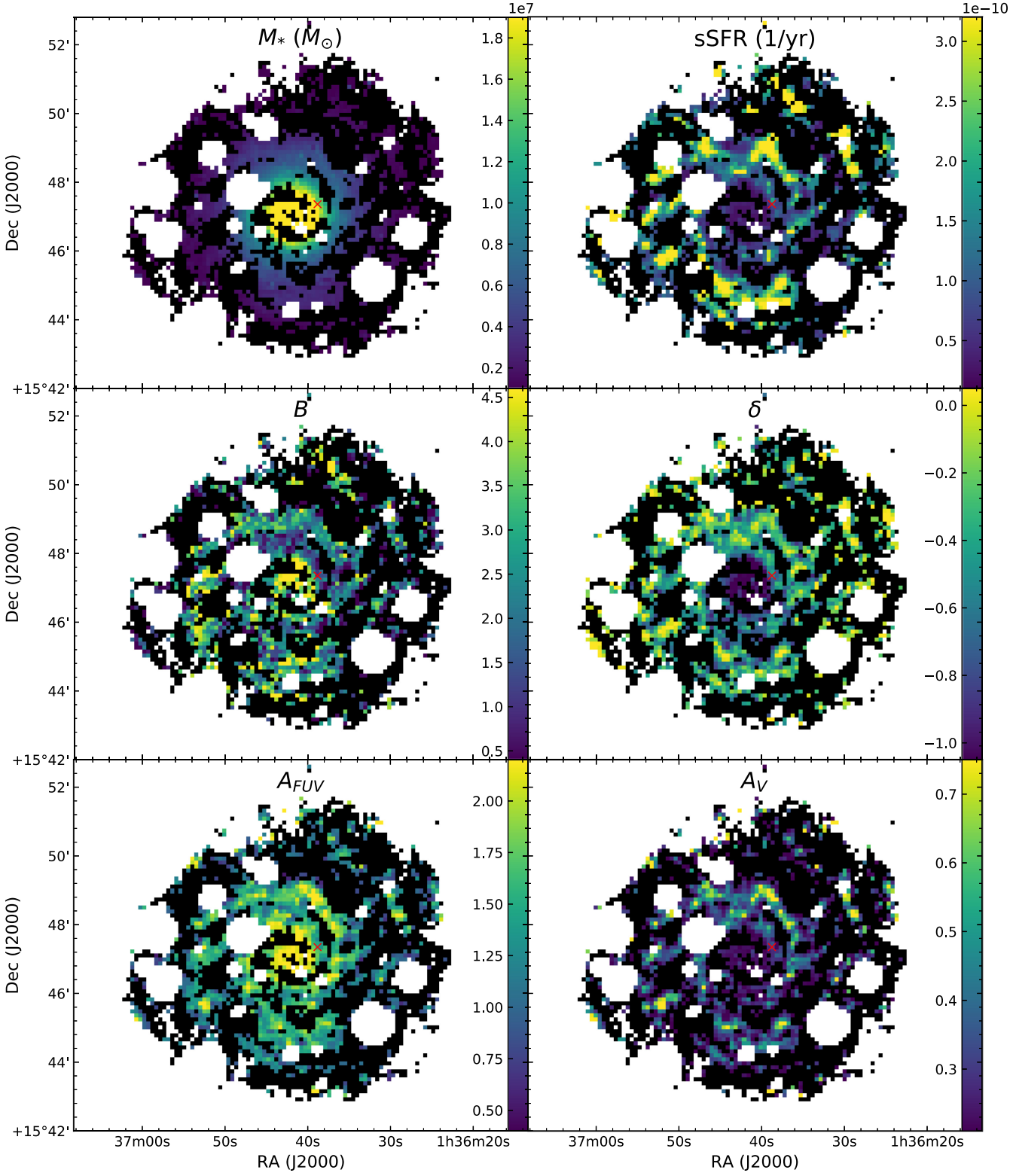

Figure 9. Maps of the stellar mass M_* (in $M_\odot$), the sSFR (in $1\,yr^{-1}$), the UV bump strength B, the attenuation slope δ, the FUV attenuation A_{FUV}, and the V-band attenuation A_V for NGC 628, all derived from the CIGALE fitting. Pixels with $A_V \leq 0.2$ are shown in black. The red cross indicates pixel 261 258 in the central spiral arm, for which the fitting results can be found in Table 2.

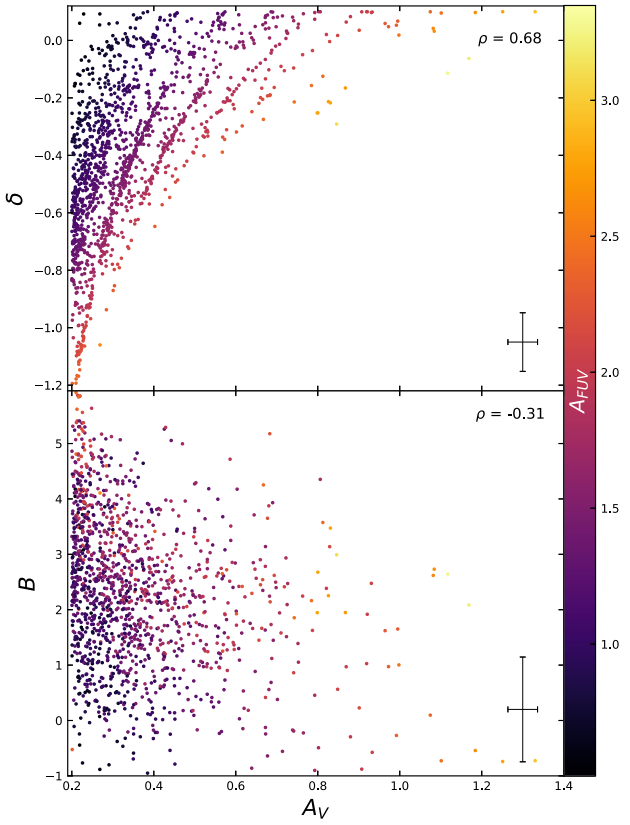

Figure 10. The attenuation curve slope δ and the bump strength B versus the V-band attenuation A_V, colour coded with the FUV attenuation A_{FUV}. Typical error bars as well as the Spearman correlation coefficient ρ are indicated.

The A_V map shows that the V-band attenuation is below 1 across the galaxy disc, in agreement with the nearly transparent discs for galaxies viewed face-on as inferred from dust radiative transfer models (e.g. Xilouris et al. 1999; Bianchi 2007; De Geyter et al. 2014; De Looze et al. 2014; Mosenkov et al. 2018).

7.2 Trends between the shape of the dust attenuation curve and other galaxy properties

In this section, we attempt to explain the observed variety in the shape of the dust attenuation curve within the galaxy by looking at possible trends between the attenuation curve properties and other galaxy properties. In the top panel of Fig. 10, we see a correlation between the slope of the attenuation curve and the V-band attenuation A_V,[14] with shallower slopes corresponding to higher A_V values. A similar trend was inferred by Hagen et al. (2017), Salim et al. (2018), Tress et al. (2018), and Narayanan et al. (2018), and interpreted in light of models presented in Chevallard et al. (2013). More specifically, in regions with higher levels of dust attenuation, dust absorption dominates over scattering processes, which results in a flattening of the dust attenuation curve. This suggests that the relative geometry of stars and dust dominates variations in the shape of the dust attenuation curve as opposed to

[14]Note that it is also possible to use the colour excess $E(B-V)$ as a measure for the amount of attenuation. However, in this case the trends are more difficult to interpret and to compare to other studies that use A_V, e.g. Hagen et al. (2017), Salim et al. (2018), and Narayanan et al. (2018).

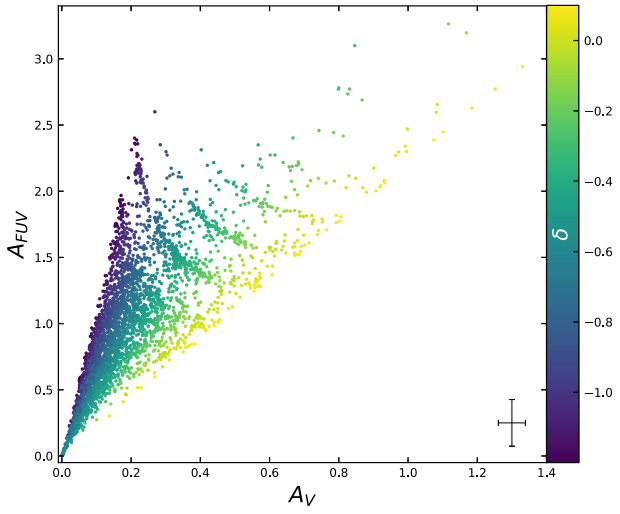

Figure 11. FUV attenuation A_{FUV} versus V-band attenuation A_V, colour coded with the attenuation slope values. Typical error bars are indicated. The 'upper' data points (in purple) correspond to the steepest slopes, whereas the 'lower' points (in yellow) correspond to the shallowest slopes.

alterations in intrinsic grain species. Narayanan et al. (2018) also conclude that the slope primarily depends on the star–dust geometry, based on simulations with 3D Monte Carlo dust radiative transfer calculations. They found that a flatter attenuation curve can be attributed to a mixed geometry with a larger fraction of unobscured young stars (decreasing the UV attenuation) and/or more obscured old stars (increasing the optical attenuation).

In the same plot, the dependence of the slope on the FUV attenuation can be seen: at a fixed A_V the slope tends to be steeper for higher A_{FUV}. This trend was also found by Salim et al. (2018) and may appear contradictory to the slope versus A_V trend, because one expects dust attenuation in the UV to follow the attenuation in the optical. However, as clearly explained in their work, this is only true if the galaxy obeys a universal attenuation law. This is also visible in the plot in Fig. 10: for a fixed slope A_{FUV} indeed increases with A_V. When there is a wide range of attenuation slopes, the A_{FUV} versus A_V correlation shows a large scatter, as can be seen in Fig. 11. The 'upper' data points correspond to the steepest slopes, whereas the 'lower' points correspond to the shallowest slopes.

The bottom panel of Fig. 10 shows a subtle trend between the bump strength and A_V, in agreement with Hagen et al. (2017), Salim et al. (2018), and Tress et al. (2018), who also found weaker bumps at higher A_V. It is possible that in our case the somewhat larger uncertainty on the derived bump strengths dilutes the correlation. Nevertheless, there is a large variation in bump strengths across the galaxy disc, as can be seen in Fig. 9. Narayanan et al. (2018) showed that the variation in bump strengths can be caused by geometry effects. They found that light scattered into the line of sight contributes modestly to reduced bump strengths, but it does not dominate. Moreover, they showed that galaxies with very complex young star–dust geometries (with a larger fraction of unobscured young stars) have reduced bumps. This can indicate that the regions in NGC 628 with weaker bumps have a significant contribution of unobscured young stars.

Plotting the slope versus the bump strength (see Fig. 12) results in a modest correlation (although there is a large scatter): steeper curves correspond to stronger bumps. A similar trend was found by Salim et al. (2018), who showed that the anticorrelation between the bump strength and slope is not driven by modelling artefacts.

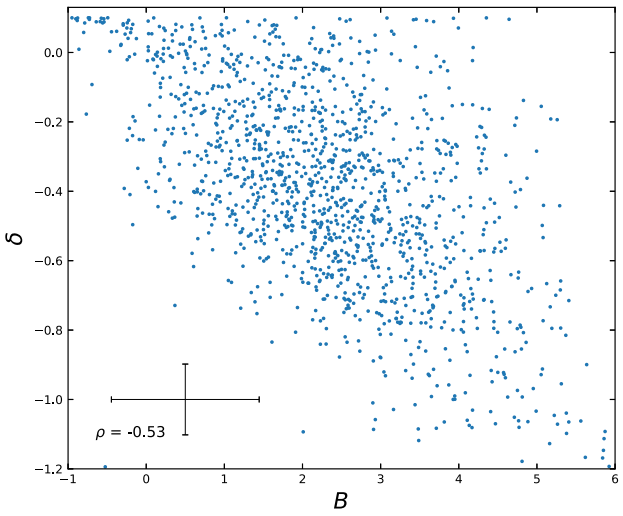

Figure 12. Attenuation slope δ versus bump strength B. Typical error bars as well as the Spearman correlation coefficient ρ are indicated.

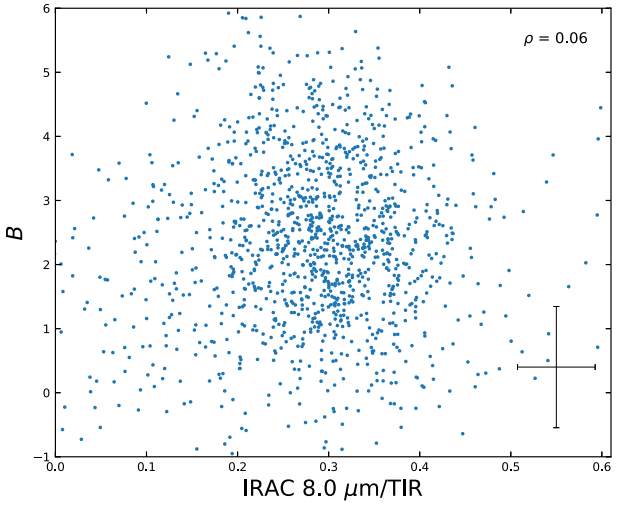

Figure 13. Bump strength B versus the IRAC 8 μm/TIR fraction. Typical error bars as well as the Spearman correlation coefficient ρ are indicated.

The same correlation was observed by Kriek & Conroy (2013) for $0.5 < z < 2.0$ galaxies and by Tress et al. (2018) for $1.5 < z < 3.0$ star-forming galaxies. However, as stated above, Narayanan et al. (2018) demonstrated that the fraction of unobscured young stars (and thus the complexity of the star–dust geometry) in their simulations correlates with *both* the slope and the bump strength of the attenuation curve, which leads to a natural relationship between both parameters. They indeed confirm that the slope varies inversely with the bump strength. Finally, Seon & Draine (2016) showed that radiative transfer effects lead to shallower attenuation curves with weaker bumps as the interstellar medium is clumpier and dustier.

Several works have pointed to PAHs as bump carriers (e.g. Li & Greenberg 1997; Draine & Li 2007; Cecchi-Pestellini et al. 2008). If so, the strength of the 2175 Å bump is expected to correlate with the emission of the mid-infrared PAH features. In Fig. 13, we show that there is no correlation between the bump strength and the IRAC 8 μm emission (corrected for stellar emission) after normalization with the TIR emission. The absence of such a correlation is consistent with the findings from Parvathi et al. (2012) and Hagen et al. (2017). We argue, however, that this result does not necessarily rule out the association of PAHs with the 2175 Å bump, as (1) the uncertainties on the bump strengths are relatively large, (2) the IRAC 8 μm is not a direct measure of the PAH abundance, and can also reflect variations in the radiation field intensity (Compiègne et al. 2010), (3) the bump strength is not a unique measure of the PAH abundance, but is convoluted with the effects of specific mixtures of small and large grains, and (4) because of the parametrization in CIGALE the bump strength does not directly correspond to the contribution of the extra attenuation due to the bump to the total attenuation at 2175 Å (Salim et al. 2018).

7.3 Empirical versus modelling results

In Section 5, we performed an empirical analysis of the *SWIFT* and *GALEX* colours, and compared them to several theoretical stellar spectra attenuated by various dust extinction/attenuation curves. The colours sensitive to the 2175 Å bump (*UVW2*−*UVM2*, *UVM2*−*UVW1*) suggest a bump strength in NGC 628 that resembles that of the MW curve, and strongly rule out the absence of a bump as in the SMC and Calzetti curves. A similar result with a median bump strength of $B = 2.31$ (in $A_V > 0.2$ regions) (with $B = 3$ for the MW) is obtained from more realistic modelling of the SFH and dust attenuation with CIGALE, although several resolved regions in the galaxy show weaker or stronger bumps. The empirical colour analysis indicates a UV slope steepness in between the MW and SMC dust extinction curves, also in agreement with the median slope value (in $A_V > 0.2$ regions) found with CIGALE: $\delta = -0.37$ (with $\delta \approx -0.45$ for the SMC and $\delta \approx -0.15$ for the MW). However, some regions in the galaxy exhibit a steeper dust attenuation curve than that of the SMC.

As already mentioned in Section 5, the SSPs used in the empirical colour analysis might not be a good approximation for the resolved stellar populations in NGC 628. Furthermore, we are attenuating these SSPs with only a few attenuation/extinction curves. When assuming a constant SFR instead of single-age SSPs, the data points in the most constraining colour plots tend to agree more with the median attenuation curve for NGC 628 obtained with CIGALE. This indicates that using a continuous SFH is a better approximation for the mix of stellar populations in a resolved galaxy region, and that a more flexible attenuation curve can better reproduce the observations. In addition, by employing the dust energy balance we can break the degeneracies between the age of the stellar populations and the attenuation. For these reasons, we are convinced that the CIGALE modelling, using a more realistic SFH, and allowing flexibility in the shape of the attenuation curve, gives us more accurate insights into the properties of the attenuation curve on resolved scales in the galaxy, compared to the empirical colour plots.

7.4 Comparison with similar studies

In this section, we consider our results in the context of earlier studies of the dust attenuation in nearby galaxies using *SWIFT* data. Hoversten et al. (2011) found strong evidence for an MW extinction curve in M81 and Holmberg IX. They looked at individual star-forming regions in both galaxies and showed that SMC and Calzetti dust laws are excluded. From the pixel-by-pixel fitting, they conclude that both the galaxies prefer MW dust across their entire discs with only a small fraction of pixels for which LMC dust is preferred.

Hutton et al. (2014) obtained for the starburst galaxy M82 a strong rejection of extinction curves traditionally used for starburst galaxies (Calzetti 2001). Overall, the standard MW extinction law is favoured. However, in their revised and more detailed study of M82 (Hutton et al. 2015), they observed a significant gradient with projected galactocentric distance, with the central starburst region showing a standard MW extinction law with a prominent bump, progressing outwards towards an extinction curve with a weaker bump and steeper slope, tending towards the SMC law. For NGC 628, on the contrary, we do not see any significant trend between bump or slope and galactocentric distance (apart from the very steep slopes in the galactic centre that might be caused by modelling artefacts). We argue that the lack of any trends with radial distance is because NGC 628 is a star-forming spiral galaxy with most star formation occurring in the spiral arms, in contrast to M82 that has a strong star-bursting core.

Hagen et al. (2017) modelled the SMC and discovered that the bump strength has a large-scale gradient across the galaxy, from weaker in the south-west to stronger in the north-east. They also confirmed that the dust extinction curve of the SMC is fairly steep.

Dong et al. (2014) presented a study of the extinction curve within the central 200 pc region of the M31 bulge. They showed that the extinction curve is generally steep in the circumnuclear region, where the metallicity is supersolar. The derived $R_V = 2.4$–2.5 is similar to the one found towards the Galactic bulge. They conclude that large dust grains are destroyed in the harsh environments of the bulge, e.g. via potential shocks from supernova explosions and/or past activities of M31, resulting in steeper curves. Although we argue that the very steep slopes in the centre of NGC 628 are possibly caused by modelling artefacts, the destruction of large grains in the bulge might also play a role. They additionally derived the extinction curves of five dusty clumps within the central region and encountered significant variations in the mid-UV: some of the extinction curves can be explained by the extinction curve model of Fitzpatrick (1999), others show an unusually strong 2175 Å bump, which is weak elsewhere in the M31 disc (Bianchi et al. 1996).

Although the sample of nearby galaxies studied on resolved scales is currently limited, the observed range of dust attenuation curves (with variable ranges of bump strengths and UV slopes) for this small set of galaxies allows us to conclude that the shape of the dust law varies from one galaxy to another, and also shows variations on resolved galactic scales. For NGC 628, we show that geometry effects possibly dominate the variations in the slopes and bump strengths across the disc of the galaxy. If this trend persists, we speculate that variations in the shape of dust attenuation curves in nearby galaxies could be driven mostly by geometrical effects. We caution, however, that the modelling techniques used in these various works make different assumptions about the SFH, the dust attenuation curves, and the stellar populations, which might impact a direct comparison of the results. A consistent study of the dust attenuation curve in a statistical sample of nearby galaxies, for which the modelling has been done in a homogeneous way within the DustKING framework, will allow us to disentangle whether variations in dust attenuation laws are driven by intrinsic grain properties, geometry effects, and/or different modelling techniques (Decleir et al., in preparation).

8 SUMMARY AND CONCLUSIONS

In this work, we studied the dust attenuation properties on resolved scales of about 325 pc in the nearby spiral galaxy NGC 628 using an FUV-to-FIR multiwavelength data set including *SWIFT* UVOT observations that probe the 2175 Å dust absorption feature. We presented a new data reduction pipeline for the *SWIFT* UVOT images, which is fully optimized for extended sources, and accounts for the coincidence loss affecting the photon-counting instrument on a pixel-by-pixel basis.

We have utilized the SED fitting code CIGALE to constrain the SFH and the shape of the dust attenuation curve (i.e. UV slope, bump strength, and dust attenuation) based on a set of photometric measurements in the FUV-to-NIR wavelength domain. In addition, we have employed the total-infrared luminosity as an extra constraint in CIGALE to limit degeneracies between the age of stellar populations and dust attenuation parameters. With this novel SED modelling technique, we were able to constrain the attenuation curve slope and bump strength reasonably well (with median relative uncertainties of 27 and 41 per cent on the slopes and bump strengths, respectively, on resolved scales).

The main conclusions of our SED modelling with CIGALE are presented here:

(i) The median attenuation curve of NGC 628 has a fairly steep slope ($\delta = -0.37 \pm 0.10$) in between that of the MW ($\delta \approx -0.15$) and the SMC ($\delta \approx -0.45$) curves and a bump ($B = 2.31 \pm 0.95$) somewhat smaller compared to the MW ($B = 3$).

(ii) The shape of the global dust attenuation law of NGC 628 (with $B = 2.24 \pm 1.16$ and $\delta = -0.55 \pm 0.15$) is not very different from the shape of the median curve from the pixel-by-pixel fitting. Thus, for this galaxy, an investigation of the attenuation curve on resolved scales gives similar results to our finding on a global galaxy scale.

(iii) Shallower slopes are observed in regions with higher levels of dust attenuation, reflecting the dominance of absorption over scattering events, resulting in a flattening of the dust law (Chevallard et al. 2013). Geometry effects seem to dominate the variations in the slope.

(iv) The weak observed trend of smaller bumps in regions with more dust attenuation (higher A_V) can also be attributed to geometry effects (Narayanan et al. 2018).

(v) There is a trend between the slope and the bump strength of the attenuation curve: steeper curves exhibit stronger bumps. Geometrical effects can lead to a natural relationship between both parameters (Narayanan et al. 2018).

(vi) No trend between the bump strength and the IRAC 8 μm/TIR ratio could be found. We argue that this does not necessarily rule out PAHs as bump carriers, if the IRAC 8 μm emission is not a good proxy of the PAH abundance and/or if the bump strength is not an accurate measure of the extra dust attenuation due to the bump at 2175 Å. In addition, the uncertainties on the bump strengths are substantial.

The median dust attenuation parameters obtained with CIGALE are mostly in line with the conclusions inferred from the empirical colour analysis (see Section 5), although with CIGALE we find a larger variety in attenuation slopes and bump strengths across the galaxy disc. We argue that the use of more complex SED models, which are able to account for a range of stellar populations (through the SFH), and a flexible parametrization of the dust law gives more accurate insights into the dust attenuation properties.

In comparison with previous resolved studies of the dust attenuation law in M81, M82, and the SMC and LMC, the bump strength in NGC 628 is consistent with the MW-type bump in M81, M82, and some regions of the SMC/LMC. The UV slope is significantly steeper than the slopes inferred for M81 and M82, but not as steep

as the average SMC curve. To understand how the dust attenuation curve varies in the nearby Universe, and how model assumptions affect the inference of dust parameters, we require a study of the dust attenuation curve in a statistical sample of nearby galaxies, for which the modelling has been done in a homogeneous way. In future work, we will extend the analysis presented here for NGC 628 to a larger sample of nearby galaxies (Decleir et al., in preparation), which will allow us to disentangle variations in the dust attenuation law from potential model biases.

ACKNOWLEDGEMENTS

We would like to thank the anonymous referee for the constructive feedback on this paper.

The authors would like to express a special thanks to Michael Brown and Alice Breeveld for their help with the calibration of the *SWIFT* images. We would also like to thank Bryan Irby and Robert Wiegand from the *SWIFT* helpdesk.

This work benefits from a PhD Fellowship of the Research Foundation – Flanders (FWO-Vlaanderen). IDL gratefully acknowledges the support of the Research Foundation – Flanders. MB was supported by MINEDUC-UA projects, code ANT 1655 and ANT 1656, and FONDECYT project 1170618.

DustPedia is a collaborative focused research project supported by the European Union under the Seventh Framework Programme (2007-2013) call (proposal no. 606847). The participating institutions are: Cardiff University, UK; National Observatory of Athens, Greece; Ghent University, Belgium; Université Paris Sud, France; National Institute for Astrophysics, Italy and CEA, France.

This research has made use of data and/or software provided by the High Energy Astrophysics Science Archive Research Center (HEASARC), which is a service of the Astrophysics Science Division at NASA/GSFC and the High Energy Astrophysics Division of the Smithsonian Astrophysical Observatory.

This research has made use of the SVO Filter Profile Service (http://svo2.cab.inta-csic.es/svo/theory/fps3/) supported from the Spanish MINECO through grant AyA2014-55216.

This research has made use of the NASA/ IPAC Infrared Science Archive, which is operated by the Jet Propulsion Laboratory, California Institute of Technology, under contract with the National Aeronautics and Space Administration.

This publication makes use of data products from the Two Micron All Sky Survey, which is a joint project of the University of Massachusetts and the Infrared Processing and Analysis Center/California Institute of Technology, funded by the National Aeronautics and Space Administration and the National Science Foundation.

We acknowledge the usage of the HyperLeda database (http://leda.univ-lyon1.fr).

REFERENCES

Aniano G., Draine B. T., Gordon K. D., Sandstrom K., 2011, PASP, 123, 1218
Baes M., Verstappen J., De Looze I., Fritz J., Saftly W., Vidal Pérez E., Stalevski M., Valcke S., 2011, ApJS, 196, 22
Baes M. et al., 2003, MNRAS, 343, 1081
Battisti A. J., Calzetti D., Chary R.-R., 2016, ApJ, 818, 13
Battisti A. J., Calzetti D., Chary R.-R., 2017a, ApJ, 840, 109
Battisti A. J., Calzetti D., Chary R.-R., 2017b, ApJ, 851, 90
Bendo G. J. et al., 2012, MNRAS, 419, 1833
Bendo G. J. et al., 2015, MNRAS, 448, 135
Bianchi L., Clayton G. C., Bohlin R. C., Hutchings J. B., Massey P., 1996, ApJ, 471, 203
Bianchi S., 2007, A&A, 471, 765
Boquien M., Buat V., Perret V., 2014, A&A, 571, A72
Boquien M., Burgarella D., Roehlly Y., Buat V., Ciesla L., Corre D., Inoue A. K., Salas H., 2019 , A&A, 622, A103
Boquien M. et al., 2012, A&A, 539, A145
Boquien M. et al., 2013, A&A, 554, A14
Boquien M. et al., 2016, A&A, 591, A6
Breeveld A. A. et al., 2010, MNRAS, 406, 1687
Bruzual G., Charlot S., 2003, MNRAS, 344, 1000
Buat V. et al., 2011, A&A, 533, A93
Buat V. et al., 2012, A&A, 545, A141
Buat V. et al., 2014, A&A, 561, A39
Calzetti D., 2001, New Astron. Rev., 45, 601
Calzetti D., Armus L., Bohlin R. C., Kinney A. L., Koornneef J., Storchi-Bergmann T., 2000, ApJ, 533, 682
Calzetti D., Kinney A. L., Storchi-Bergmann T., 1994, ApJ, 429, 582
Camps P., Baes M., 2015, Astron. Comput., 9, 20
Cardelli J. A., Clayton G. C., Mathis J. S., 1989, ApJ, 345, 245
Cartledge S. I. B. et al., 2005, ApJ, 630, 355
Cecchi-Pestellini C., Malloci G., Mulas G., Joblin C., Williams D. A., 2008, A&A, 486, L25
Chabrier G., 2003, PASP, 115, 763
Charlot S., Fall S. M., 2000, ApJ, 539, 718
Chevallard J., Charlot S., Wandelt B., Wild V., 2013, MNRAS, 432, 2061
Ciesla L., Elbaz D., Fensch J., 2017, A&A, 608, A41
Clark C. J. R. et al., 2018, A&A, 609, A37
Clayton G. C., Gordon K. D., Bianchi L. C., Massa D. L., Fitzpatrick E. L., Bohlin R. C., Wolff M. J., 2015, ApJ, 815, 14
Clayton G. C., Wolff M. J., Sofia U. J., Gordon K. D., Misselt K. A., 2003, ApJ, 588, 871
Cohen M., Megeath S. T., Hammersley P. L., Martín-Luis F., Stauffer J., 2003, AJ, 125, 2645
Compiègne M., Flagey N., Noriega-Crespo A., Martin P. G., Bernard J.-P., Paladini R., Molinari S., 2010, ApJ, 724, L44
Conroy C., Schiminovich D., Blanton M. R., 2010, ApJ, 718, 184
Dale D. A., Helou G., Magdis G. E., Armus L., Díaz-Santos T., Shi Y., 2014, ApJ, 784, 83
Davies J. I. et al., 2017, PASP, 129, 044102
De Geyter G., Baes M., Camps P., Fritz J., De Looze I., Hughes T. M., Viaene S., Gentile G., 2014, MNRAS, 441, 869
De Looze I. et al., 2014, A&A, 571, A69
Dong H. et al., 2014, ApJ, 785, 136
Draine B. T., 1978, ApJS, 36, 595
Draine B. T., Li A., 2007, ApJ, 657, 810
Draine B. T., Malhotra S., 1993, ApJ, 414, 632
Driver S. P., Popescu C. C., Tuffs R. J., Liske J., Graham A. W., Allen P. D., de Propris R., 2007, MNRAS, 379, 1022
Fitzpatrick E. L., 1999, PASP, 111, 63
Galametz M. et al., 2013, MNRAS, 431, 1956
Gehrels N. et al., 2004, ApJ, 611, 1005
Gordon K. D., Clayton G. C., Misselt K. A., Landolt A. U., Wolff M. J., 2003, ApJ, 594, 279
Gould R. J., Salpeter E. E., 1963, ApJ, 138, 393
Hagen L. M. Z., Siegel M. H., Hoversten E. A., Gronwall C., Immler S., Hagen A., 2017, MNRAS, 466, 4540
Hirashita H., Harada N., 2017, MNRAS, 467, 699
Holwerda B. W., Böker T., Dalcanton J. J., Keel W. C., de Jong R. S., 2013, MNRAS, 433, 47
Hoversten E. A. et al., 2011, AJ, 141, 205

Hughes A. et al., 2013, ApJ, 779, 46
Hunt L. K. et al., 2018, A&A, 621, A51
Hutton S., Ferreras I., Wu K., Kuin P., Breeveld A., Yershov V., Cropper M., Page M., 2014, MNRAS, 440, 150
Hutton S., Ferreras I., Yershov V., 2015, MNRAS, 452, 1412
Inoue A. K., 2011, MNRAS, 415, 2920
Karczewski O. Ł. et al., 2013, MNRAS, 431, 2493
Keel W. C., Manning A. M., Holwerda B. W., Lintott C. J., Schawinski K., 2014, AJ, 147, 44
Kennicutt Jr. R. C. et al., 2003, PASP, 115, 928
Kennicutt R. C. et al., 2011, PASP, 123, 1347
Kreckel K., Groves B., Bigiel F., Blanc G. A., Kruijssen J. M. D., Hughes A., Schruba A., Schinnerer E., 2017, ApJ, 834, 174
Kriek M., Conroy C., 2013, ApJ, 775, L16
Kuin N. P. M., Rosen S. R., 2008, MNRAS, 383, 383
Lagache G., Puget J.-L., Dole H., 2005, ARA&A, 43, 727
Leja J., Johnson B. D., Conroy C., van Dokkum P. G., Byler N., 2017, ApJ, 837, 170
Li A., Greenberg J. M., 1997, A&A, 323, 566
Lo Faro B., Buat V., Roehlly Y., Alvarez-Marquez J., Burgarella D., Silva L., Efstathiou A., 2017, MNRAS, 472, 1372
Madau P., Dickinson M., 2014, ARA&A, 52, 415
Makarov D., Prugniel P., Terekhova N., Courtois H., Vauglin I., 2014, A&A, 570, A13
Monet D. G. et al., 2003, AJ, 125, 984
Morrissey P. et al., 2007, ApJS, 173, 682
Mosenkov A. V. et al., 2018, A&A, 616, A120
Narayanan D., Conroy C., Davé R., Johnson B. D., Popping G., 2018, ApJ, 869, 70
Noll S., Burgarella D., Giovannoli E., Buat V., Marcillac D., Mu noz-Mateos J. C., 2009, A&A, 507, 1793
Panuzzo P., Granato G. L., Buat V., Inoue A. K., Silva L., Iglesias-Páramo J., Bressan A., 2007, MNRAS, 375, 640
Parvathi V. S., Sofia U. J., Murthy J., Babu B. R. S., 2012, ApJ, 760, 36
Poggianti B. M., Bressan A., Franceschini A., 2001, ApJ, 550, 195
Poole T. S. et al., 2008, MNRAS, 383, 627
Reddy N. A. et al., 2015, ApJ, 806, 259
Roehlly Y., Burgarella D., Buat V., Boquien M., Ciesla L., Heinis S., 2014, in Manset N., Forshay P., eds, ASP Conf. Ser. Vol. 485, Astronomical Data Analysis Software and Systems XXIII. Astron. Soc. Pac., San Francisco, p. 347
Roming P. W. A. et al., 2005, Space Sci. Rev., 120, 95
Rémy-Ruyer A. et al., 2014, A&A, 563, A31
Salim S., Boquien M., Lee J. C., 2018, ApJ, 859, 11
Salmon B. et al., 2016, ApJ, 827, 20
Seon K.-I., Draine B. T., 2016, ApJ, 833, 201
Skrutskie M.F., et al., 2006, AJ, 131, 1163
Tress M. et al., 2018, MNRAS, 475, 2363
Valencic L. A., Clayton G. C., Gordon K. D., 2004, ApJ, 616, 912
Viaene S. et al., 2014, A&A, 567, A71
Viaene S. et al., 2016, A&A, 586, A13
Wild V., Charlot S., Brinchmann J., Heckman T., Vince O., Pacifici C., Chevallard J., 2011, MNRAS, 417, 1760
Xilouris E. M., Byun Y. I., Kylafis N. D., Paleologou E. V., Papamastorakis J., 1999, A&A, 344, 868

APPENDIX A: IDS OF *SWIFT* UVOT IMAGES

Table A1 lists the IDs of the *SWIFT* UVOT images that were used in this work (see Section 3.1 for more information). Note that each of these 'images' contains several individual frames that need to be reduced separately.

Table A1. Image IDs of the *SWIFT* UVOT images that were used in this work.

Epoch	Filter	Prefix	Image IDs
2007	*UVW2*	sw000365680	01
	UVM2	sw000365680	01
	UVW1	sw000365680	01
2008	*UVW2*	sw000358680	01, 02
	UVM2	sw000358680	01, 02
	UVW1	sw000358680	01, 02
2013	*UVW2*	sw000328910	01, 02, 03, 06, 09, 11, 14, 15, 16, 19, 20, 21, 22, 23, 24, 25, 27, 29, 31, 33, 35, 37, 39, 40, 42, 43, 45, 46, 47
	UVM2	sw000328910	01, 02, 12, 17, 18, 19, 21, 22, 23, 25, 27, 29, 31, 33, 35, 37, 40, 42, 43, 45, 46, 47
	UVW1	sw000328910	03, 10, 19, 20, 21, 22, 23, 24, 25, 27, 29, 31, 33, 35, 37, 40, 42, 45
2015	*UVW2*	sw000365680	03
	UVW1	sw000365680	02

APPENDIX B: CALCULATION OF THE COINCIDENCE LOSS CORRECTION

Since the existing calculations of coincidence loss corrections in *SWIFT* UVOT images are not feasible for pixel-by-pixel studies of extended sources, as described in Section 3.4.1, we had to come up with a new strategy. We adjusted the correction technique for point sources of Poole et al. (2008) to a pixel-by-pixel algorithm. Because of the photon splash that is created in the detector, one cannot simply calculate a correction factor for each individual pixel without taking into account the surrounding pixels. Therefore, we determine the coincidence loss correction factor within a 9×9 pixel sized box (or 81 arcsec^2 in our case) centred on the pixel of interest, which covers an area equivalent to an $R = 5$ arcsec aperture region. The coincidence-loss-corrected count rate $C_{\rm coicorr}$ (in counts s^{-1}) in a certain pixel is calculated as

$$C_{\rm coicorr} = C_{\rm obs} \times f_{\rm coicorr}, \tag{B1}$$

where $C_{\rm obs}$ is the observed count rate in that pixel and $f_{\rm coicorr}$ is the coincidence loss correction factor determined within a 9×9 pixel sized box centred on that pixel. Following the prescriptions by Poole et al. (2008), the correction can be calculated as follows.

The theoretical coincidence-loss-corrected count rate $C_{\rm theory\square}$[15] (in counts s^{-1}) in a 9×9 pixel box is

$$C_{\rm theory\square} = \frac{-\ln(1 - \alpha\, C_{\rm raw\square}\, f_t)}{\alpha\, f_t}, \tag{B2}$$

where $C_{\rm raw\square}$ is the raw observed count rate in the 9×9 pixel box. f_t is the frame time (0.011 03 s for a full frame; keyword FRAMTIME in the FITS file header) and α is the dead time correction factor (1 minus the dead time fraction; 0.9842 for a full frame; keyword DEADC in the FITS file header). As already explained, this theoretical coincidence loss expression cannot be applied on a pixel-by-pixel basis because every photon count is assigned to a certain pixel by centroiding a photon splash that was

[15]The $\square$ indicates that we are working in a 9×9 pixel sized box.

spread over five physical CCD pixels. To compensate for this, we need to use the empirical polynomial correction from Poole et al. (2008) to account for the differences between the observed and theoretical coincidence loss correction:

$$f(x) = 1 + a_1 x + a_2 x^2 + a_3 x^3 + a_4 x^4, \quad \text{(B3)}$$

where $x = C_{\text{raw}\square} f_t$. The coefficients in this equation are taken from table 1 of the *SWIFT* UVOT CALDB Release Note 14-R02.[16] The full coincidence-loss-corrected incident count rate in the 9×9 pixel box $C_{\text{corr}\square}$ (in counts s^{-1}) is then

$$C_{\text{corr}\square} = C_{\text{theory}\square} \times f(x). \quad \text{(B4)}$$

The coincidence loss correction factor f_{coicorr} in the central pixel of the box is then eventually

$$f_{\text{coicorr}} = \frac{C_{\text{corr}\square}}{C_{\text{raw}\square}}. \quad \text{(B5)}$$

We refer the reader to section 7 of Poole et al. (2008) for more details on the calculation.

To get an estimate of the uncertainty on the coincidence loss correction, we determine the standard deviation on the count rate $\sigma_\square$ in each 9×9 pixel box. Following the same procedure as above, we calculate a 'minimum' correction factor, based on a minimum count rate in the box $C_{\text{min}\square} = C_{\text{raw}\square} - 81 \times \sigma_\square$ and a 'maximum' correction factor, based on a maximum count rate $C_{\text{max}\square} = C_{\text{raw}\square} + 81 \times \sigma_\square$. Subsequently, we compute the difference between the coincidence-loss-corrected flux and the minimum/maximum corrected flux in every pixel. The largest of these two differences can be considered as an upper limit of the uncertainty on the corrected flux. In our case, typical uncertainties are extremely small (<0.2 per cent) compared to other sources of uncertainty and can therefore safely be neglected.

APPENDIX C: PARAMETER RANGES USED IN THE CIGALE FITTING

Table C1 lists the parameters that were used in the CIGALE fitting, with a range of values in the case of free parameters or with one value in the case of fixed parameters.

APPENDIX D: OBSERVATIONS, MODELS, AND RESIDUALS FOR ALL WAVEBANDS FITTED WITH CIGALE

Fig. D1 shows the observations, the models, and the residuals for the 15 wavebands that were fitted with CIGALE. Residuals are calculated as the relative difference between the modelled and the observed flux. In the histograms of the residuals, we draw vertical lines at typical uncertainties on the observed flux, e.g. around 7 per cent for the *FUV*- band. Overall, the observations are fitted quite well with residuals within the typical uncertainties on the observed flux. In the *SWIFT UVW2* and *UVW1*-bands, the model slightly underestimates the observations (negative residuals), with the largest offsets (around 15 per cent) in the interarm regions where the uncertainties on the flux are larger (lower SNR). The SDSS *z*-band shows a somewhat larger offset compared to the other optical bands, which might be due to issues with the background subtraction in this image. Finally, the 2MASS bands are fitted quite well in the central regions of the galaxy, but worse in the outer regions due to a lower SNR. Typical uncertainties on the observed fluxes in these bands are also very high (36–90 per cent on average).

[16] https://heasarc.gsfc.nasa.gov/docs/heasarc/caldb/swift/docs/uvot/uvot_caldb_coi_02.pdf

Table C1. Parameter ranges used in the CIGALE fitting for the SFH: the e-folding time of the main stellar population model τ_{main} (in Myr), the age of the oldest stars in the galaxy a (in Myr), the age of the drop in the star formation activity a_{trunc} (in Myr), the ratio between the SFR after and before truncation r_{sfr}, the multiplicative factor controlling the amplitude of SFR A_{sfr}, and the normalization flag *norm* to normalize the SFH to produce one solar mass; and the dust attenuation: the amplitude of the UV bump B, the power-law slope δ, the colour excess of the stellar continuum light $E(B-V)$, the reduction factor for the colour excess of the old population compared to the young one $E(B-V)_{\text{old factor}}$, the central wavelength of the UV bump λ (in nm), and the width of the UV bump *FHWM* (in nm). All other (fixed) parameter values are also given: the initial mass function *IMF*, the metallicity Z, the age separation between the young and old stellar populations a_{sep} (in Myr), the ionization parameter of the nebular emission $\log(U)$, the fraction of Lyman continuum photons escaping the galaxy f_{esc}, the fraction of Lyman continuum photons absorbed by dust f_{dust}, the line width *lw* (in km s^{-1}), the flag *em* whether or not to include nebular emission, the AGN fraction f_{AGN}, the slope of the DALE2014 dust emission templates α, and the redshift z.

SFH parameters	
τ_{main}	500, 1000, 2000, 4000, 5000, 6000, 7000, 8000
a	8000, 9000, 10 000, 11 000, 12 000
a_{trunc}	100
r_{sfr}	0, 0.001, 0.01, 0.02, 0.05, 0.075, 0.1, 0.2, 0.5, 0.75, 1, 2, 5, 7.5, 10
A_{sfr}	1
norm	True
Dust attenuation parameters	
B	−1, −0.5, 0, 0.5, 1, 1.5, 2, 2.5, 3, 3.5, 4, 4.5, 5, 5.5, 6
δ	−1.2, −1.15, −1.1, −1.05, −1, −0.95, −0.9, −0.85, −0.8, −0.75, −0.7, −0.65, −0.6, −0.55, −0.5, −0.45, −0.4, −0.35, −0.3, −0.25, −0.2, −0.15, −0.1, −0.05, 0, 0.05, 0.1
$E(B-V)$	0, 0.01, 0.02, 0.03, 0.04, 0.05, 0.06, 0.07, 0.08, 0.09, 0.1, 0.125, 0.15, 0.175, 0.2, 0.225, 0.25, 0.275, 0.3, 0.325, 0.35, 0.375, 0.4, 0.425, 0.45, 0.475, 0.5
$E(B-V)_{\text{old factor}}$	1
λ	217.5
FWHM	35
Other (fixed) parameters	
IMF	1 (Chabrier)
Z	0.02
a_{sep}	10
$\log(U)$	−3.0
f_{esc}	0
f_{dust}	0
lw	300
em	True
f_{AGN}	0
α	2
z	0

APPENDIX E: MOCK TESTING WITH CIGALE

In order to verify whether our CIGALE model is able to constrain physical properties such as the SFR and the shape of the dust

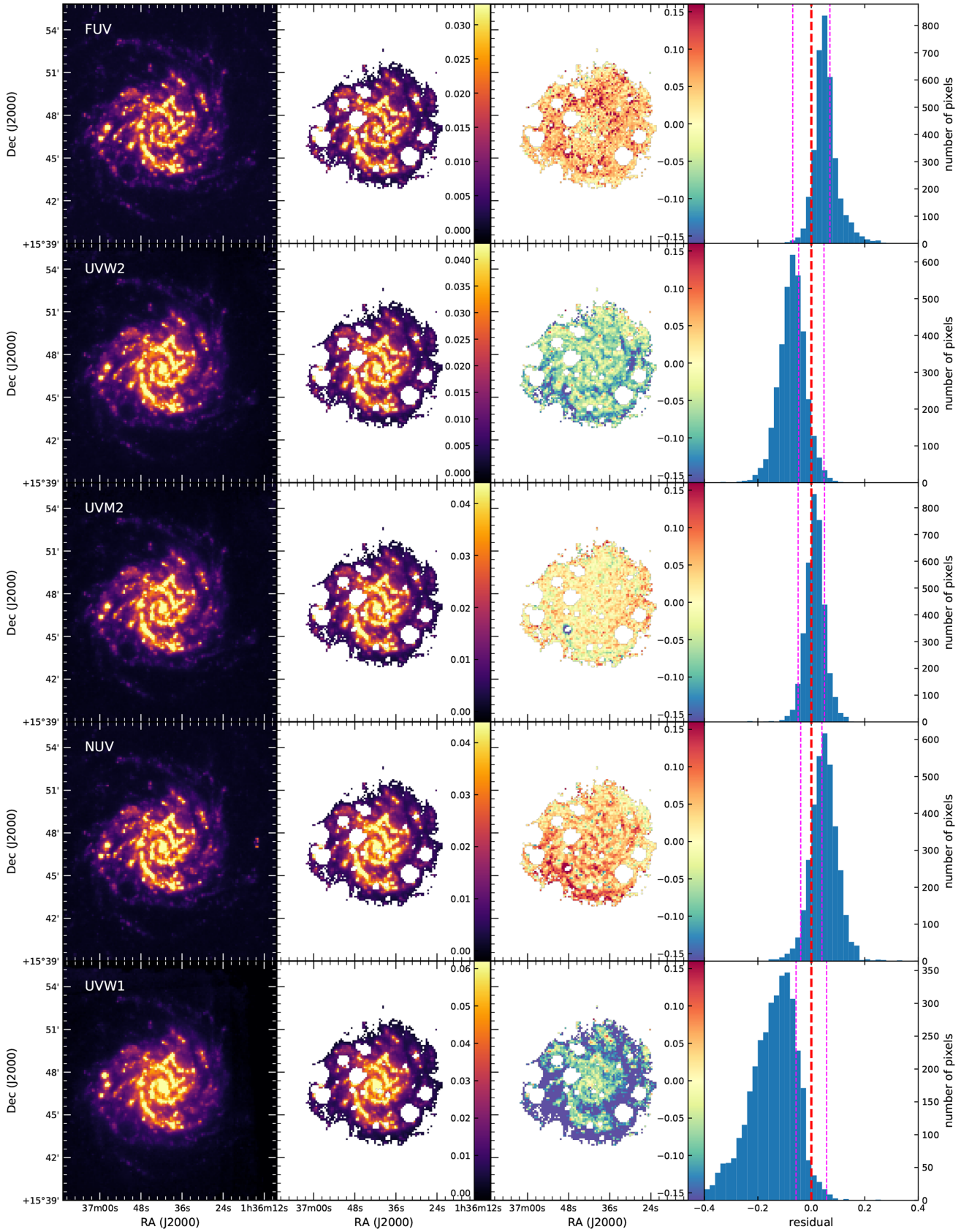

Figure D1. From left to right: Observation and model maps (in MJy sr^{-1}), residual map, and histogram of the residual for the UV bands fitted with CIGALE. The white regions within the galaxy models and residuals are masked pixels of foreground stars that were left out from the fitting. The dashed magenta lines in the histograms represent the median uncertainty on the observed flux.

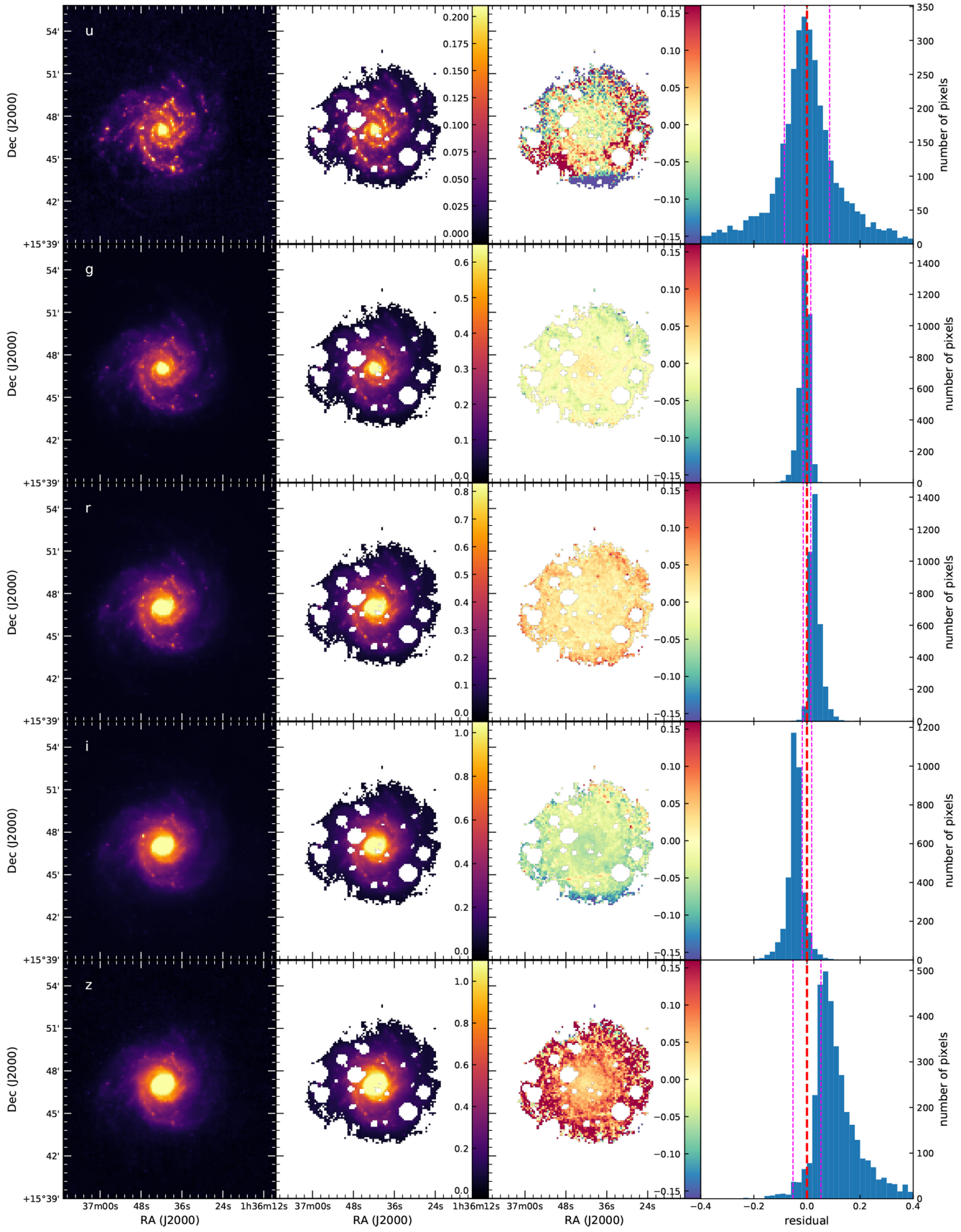

Figure D1 – *Continued*

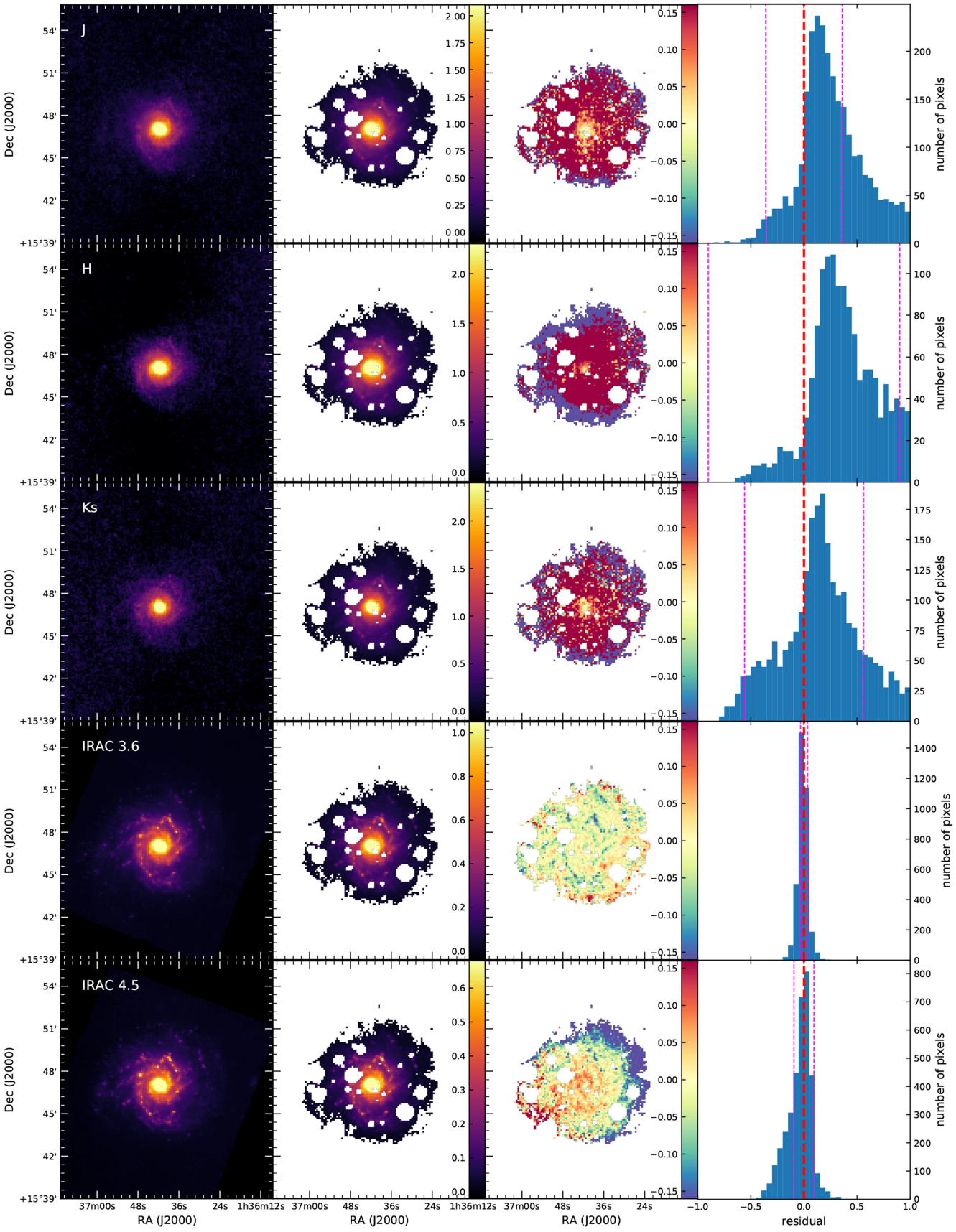

Figure D1 – *Continued*

attenuation curve, we performed a mock data analysis with input data generated from model SEDs for which we know the true parameters and by assuming the same noise levels that affect our observations in each waveband. To this aim, we followed a similar procedure as in appendix B.2 of Boquien et al. (2016). We start from the SED and the associated physical properties of the best-fitting model obtained for NGC 628. A random Gaussian noise is added to the flux in each band, based on the 1σ uncertainty on the observed fluxes, to simulate an observation of the SED. In a second step, this simulated observation is fitted with the Bayesian approach of CIGALE. In Fig. E1, we compare the 'true' (input) and 'estimated' (output) values for the UV bump strength B, the attenuation slope δ, the SFR, and the FUV attenuation $A_{\rm FUV}$.

It is clear that the SFR and the $A_{\rm FUV}$ are constrained well; all mock models are concentrated along the one-to-one correlation with a scatter of only 0.12 on the $\log(\mathrm{SFR}(\mathrm{M}_\odot\ \mathrm{yr}^{-1}))$ and 0.25 on the $A_{\rm FUV}$. On the other hand, the bump strength and UV slope seem to be more difficult to reproduce. However, ignoring pixels with an $A_{\rm V} \leq 0.2$ (indicated in black in Fig. E1) significantly improves the constraints on these parameters, with the scatter around the one-to-one relation on the bump strength decreasing from 1.88 to 1.23, and on the slope from 0.28 to 0.18. For those pixels with a very low dust attenuation, it is essentially impossible to get meaningful constraints on the attenuation curve. In addition, we applied a correction to the images to account for the Galactic foreground extinction of $A_{\rm V} = 0.188$ (see Section 4). This will add noise to the data points, making them less reliable, especially for pixels with $A_{\rm V} \leq 0.2$. The results improve further with increasing $A_{\rm V}$: the scatter on the bump, e.g. decreases to 0.90 if we only consider mock data points with $A_{\rm V} > 0.5$, and on the slope to 0.09. Due to the non-negligible uncertainties on the resolved *SWIFT* fluxes (4.5–6 per cent on average), it is not surprising that the bump strength is only well constrained for pixels with a sufficiently high dust attenuation. Therefore, we are confident that the model is able to constrain all properties within reasonable uncertainties.

In the first mock test (see Fig. E1), we have used the same set-up for the SFH for both the generation and the fitting of the mock data in CIGALE, which does not allow us to test the influence of our assumed SFH. To check the dependence of the results on the model SFH (in addition to the test explained in Section 6.3), we also performed a 'hybrid' mock data analysis in which we start from the best model for NGC 628 obtained with a double exponential SFH (SFH2EXP) to create a mock data set, which is subsequently fitted using the delayed and flexible SFH (SFHDELAYEDFLEX). The

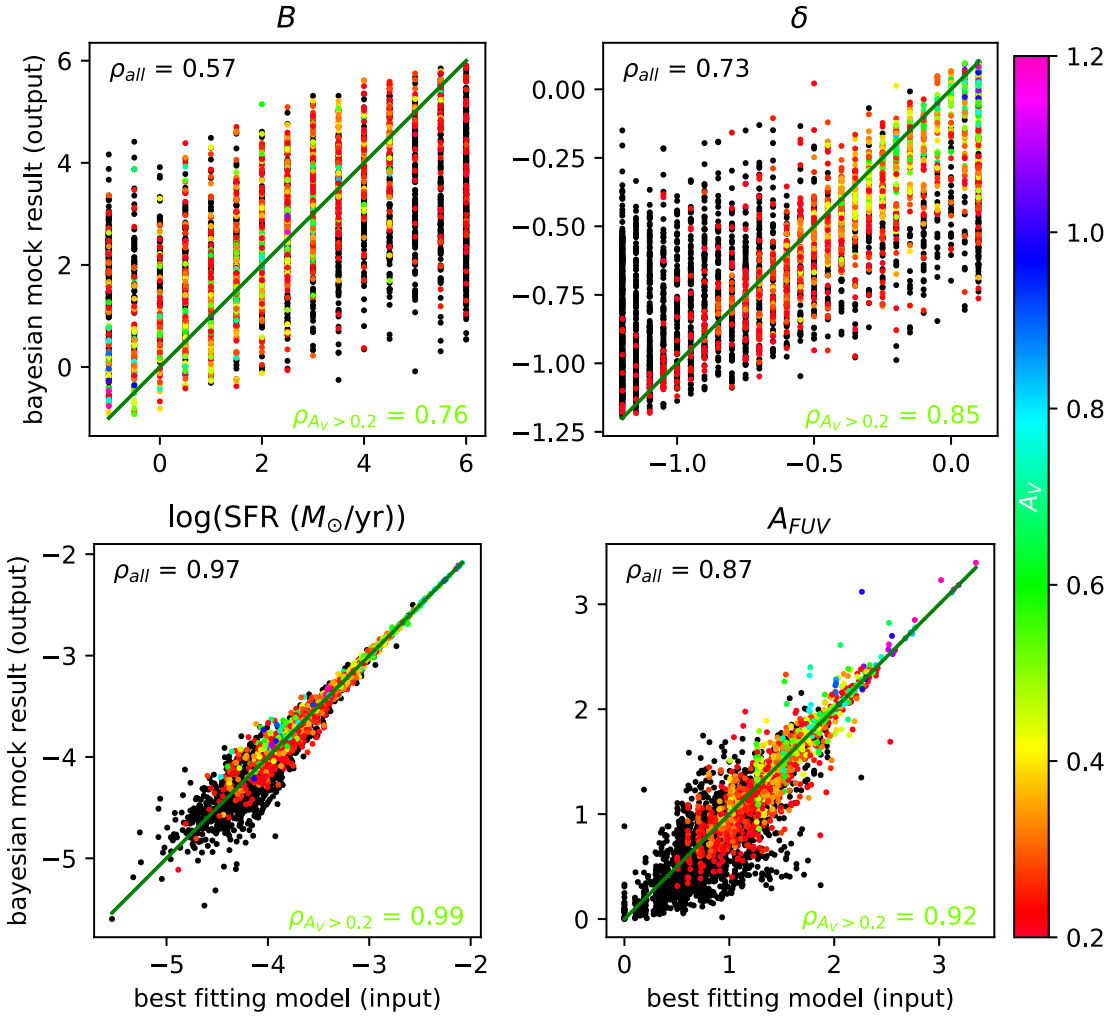

Figure E1. Mock data analysis results for the UV bump strength B, the attenuation slope δ, the SFR (in $\mathrm{M}_\odot\ \mathrm{yr}^{-1}$), and the FUV attenuation $A_{\rm FUV}$. The black dots represent pixels with $A_{\rm V} \leq 0.2$. The Spearman correlation coefficient ρ is shown for all pixels (in black) and for pixels with $A_{\rm V} > 0.2$ (in green).

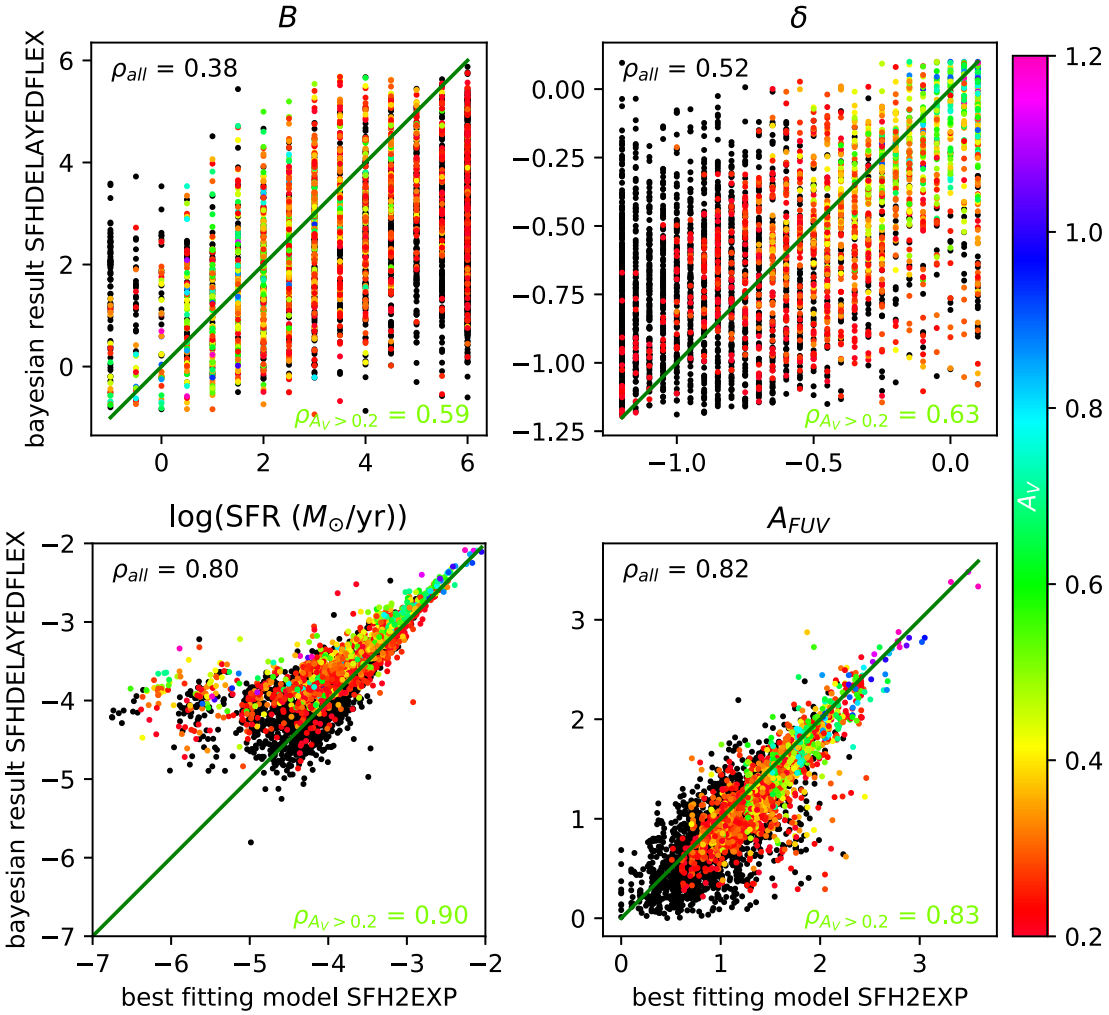

Figure E2. Mock data analysis results for the UV bump strength B, the attenuation slope δ, the SFR (in $M_\odot\ yr^{-1}$), and the FUV attenuation A_{FUV}, for the hybrid approach as explained in the text. The black dots represent pixels with $A_V \leq 0.2$. The Spearman correlation coefficient ρ is shown for all pixels (in black) and for pixels with $A_V > 0.2$ (in green).

comparison between the 'true' and 'estimated' properties is given in Fig. E2. The A_{FUV} is again constrained very well with a scatter of 0.31 around the one-to-one correlation, while there is somewhat more scatter (0.60) on the log(SFR($M_\odot\ yr^{-1}$)). The bump and the slope show substantial scatter (2.32 and 0.35, respectively), which improves down to a dispersion of 1.02 on the bump and 0.15 on the slope considering only models with $A_V > 0.5$. The larger scatter on the SFR indicates that our assumption on the SFH will affect the modelling of the unattenuated stellar population, which will in turn alter the derivation of the dust attenuation curve parameters. For pixels with $A_V > 0.5$, the SFR and UV slope are reproduced relatively well, whereas the bump strength is more difficult to constrain. This hybrid mock analysis demonstrates that the assumed SFH has an influence on the results. However, as explained in Section 6.3, we argue that the delayed and flexible SFH is more adequate to model the resolved regions in NGC 628 compared to the double exponentially declining SFH. The delayed SFH with a final burst/quench is better adapted because it can more easily represent the more diverse SFHs we expect at a local scale in the galaxy disc: spiral arms had a recent episode of star formation, whereas the star formation in interarm regions has fallen. This cannot be obtained with a double exponentially declining SFH.

This paper has been typeset from a TEX/LATEX file prepared by the author.